Table 1
Serum iron concentration in rats after intravenous injection of SPIO-low dose (109.5 μmol Fe/kg), SPIO-high dose (218.9 μmol Fe/kg), 1 mL 0.6% (w/v) alginate solution, and saline. The basic serum iron concentration before administration was 10.64 ± 4.58 μg/mL. Data represent mean ± S.D.

Time (h)	SPIO-low dose	SPIO-high dose	Alginate solution	Saline
0	9.32 ± 5.55	9.08 ± 3.42	10.96 ± 4.73	21.09 ± 6.13
0.083	143.75 ± 18.61	356.10 ± 42.82	6.16 ± 1.52	15.75 ± 3.71
0.167	131.90 ± 13.56	310.44 ± 64.55	5.48 ± 0.57	15.01 ± 1.18
0.5	57.62 ± 19.43	183.87 ± 37.37	7.49 ± 0.88	17.23 ± 2.23
1	19.57 ± 10.82	108.28 ± 38.23	8.52 ± 3.07	10.80 ± 1.88
3	8.74 ± 5.29	19.83 ± 15.31	6.86 ± 2.08	12.51 ± 5.25
6	6.79 ± 3.20	8.68 ± 5.36	4.72 ± 1.61	9.71 ± 0.92
12	3.28 ± 1.01	3.89 ± 2.13	6.96 ± 3.54	6.48 ± 1.23
24	4.52 ± 1.43	3.01 ± 1.75	5.07 ± 1.29	ND

ND: not determined.

the blood iron concentrations in all rats were even under the initial concentration before injection between 6 and 48 h after injection.

The basic serum iron concentration before administration fluctuated between 6.06 and 15.22 μg/mL. The serum iron concentrations at various time points after injection of alginate solution and saline located in the range of basic serum iron concentration (Table 1). But, the serum iron concentrations increased significantly after SPIO-alginate injection and then decreased to the basic serum iron concentration range at 3 h for low dose and at 6 h for high dose. The $T_{1/2}$ of SPIO-alginate was 0.27 ± 0.06 h at low dose and 0.65 ± 0.22 h at high dose calculated by noncompartmental analysis (Table 2).

3.2. Tissue distribution of SPIO-alginate in normal rats

Table 3 showed that the iron concentrations in liver and spleen significantly increased, while those in blood, lungs, heart, and kidneys slightly changed after injection of SPIO-alginate at low dose. Considering the weights of organs, the results revealed that more than 80% of the injected iron accumulated into the liver, and about 10% into the spleen while less than 2% was found in the kidneys, heart and lungs, respectively. The iron concentrations in the liver and the spleen were high between 0.5 and 24 h, and began to decrease after 24 h. The tissue distribution parameters in liver and spleen for SPIO-alginate in rat calculated by the WinNonlin program using noncompartmental model was given in Table 2. It indicated that the elimination of iron in liver was slower than that in spleen.

3.3. Histological evaluation in normal rat

Although the experiments were carried out at different time points before and after injection of SPIO-alginate as described in methods, only the typical micrographs were shown in order to shorten the length of writing. HE staining could reflect the effect of SPIO-alginate on the morphology of tissues. The sections indicated that there was no significant change on the basic structure of all the specimens of liver and spleen, though there was a little edema of hepatocytes in the perimeter section of liver lobules (Fig. 1).

Perls staining was performed to detect the iron particles dyed blue. Stainable iron was observed in KCs in hepatic sinusoid, in splenic cord of the perimeter section of follicle and in splenic red pulp at 0.5, 24, 96, and 336 h after injection of low dose of SPIO-alginate (Fig. 1). Additionally, iron particles were distributed in the perimeter section of liver lobules at 0.5 h and in the center section at 96 h. The amount of iron oxide particles in liver qualitatively peaked between 0.5 and 24 h after injection, and small amounts of particles were still present at 336 h after injection. The results in the spleen were similar to those in the liver.

Table 2
Serum, liver and spleen parameters of SPIO-alginate in rats following intravenous injection at 109.5 and 218.9 μmol Fe/kg using noncompartmental analysis with bolus IV administration for serum and extravascular administration for liver and spleen

Parameters	Serum ($n = 5$)		Liver	Spleen
	Low dose	High dose	Low dose	Low dose
T_{max} (h)	0.083	0.083, 0.176	0.5	24
C_{max} (μg/mL or g)	147.91 ± 20.72	348.99 ± 43.78*	176.64	290.06
λ (h^{-1})[a]	2.95 ± 0.87	1.28 ± 0.40*	0.005	0.0085
AUC_{0-24h} (h μg/mL or h μg/g)[b]	68.37 ± 18.87	321.74 ± 123.72*	35,176.83	26,307.97
$T_{1/2}$ (h)	0.25 ± 0.06	0.59 ± 0.20*	139.19	81.98
MRT_{0-24h} (h)	0.32 ± 0.11	0.76 ± 0.27*	181.179	86.235

Each value of serum parameter represents the mean ± S.D.
[a] $T_{1/2}$ was calculated from the terminal slope by means of log-linear regression.
[b] AUC was calculated by linear trapezoidal rule.
* $P < 0.05$, compared with the value of low dose in serum.

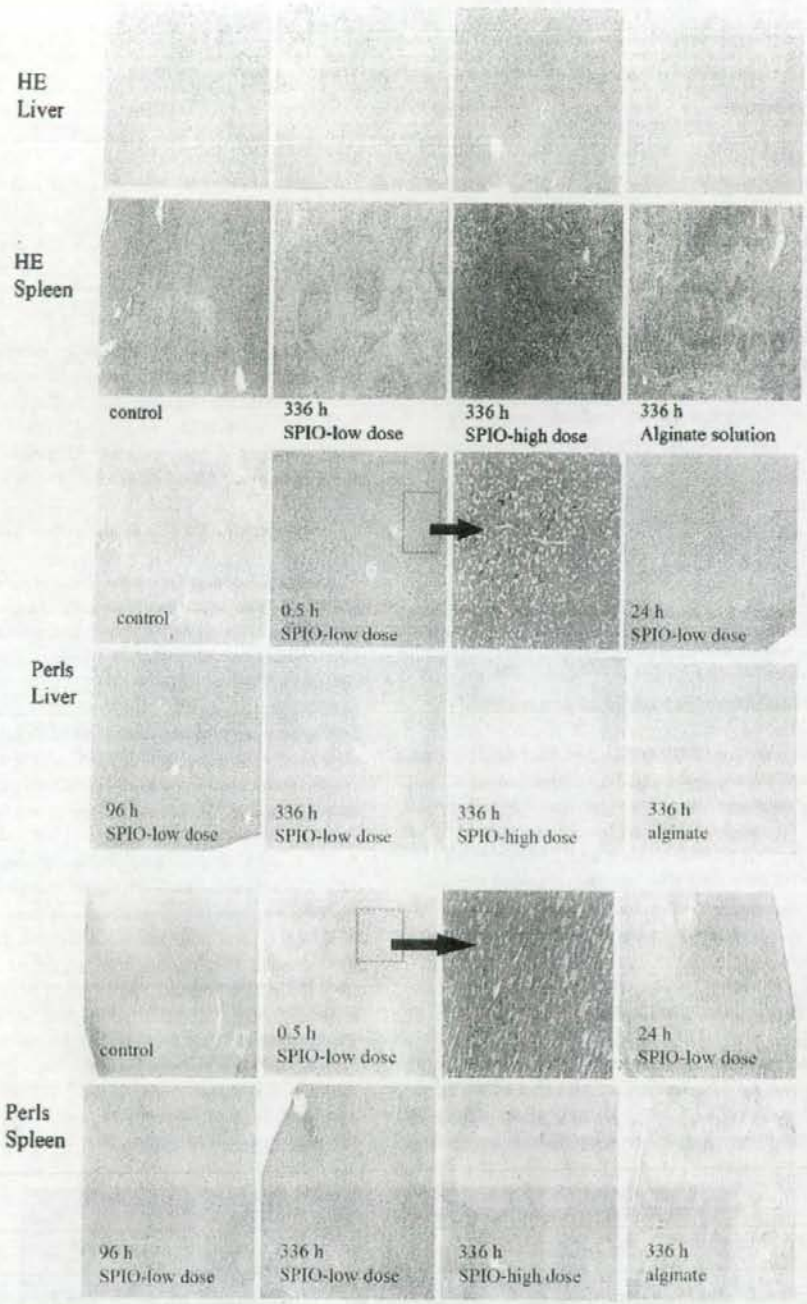

Fig. 1. Sections of liver and spleen of normal rat with HE staining and Perls staining (magnification ×10).

Table 3
Iron concentration in different tissues at different timepoints after intravenous injection of SPIO-low dose (109.5 μmol Fe/kg). Data represent mean ± S.D. ($n = 3$)

Time (h)	Iron concentrations in tissue (μg Fe/mL in whole blood; μg Fe/kg in heart, liver, spleen, lung, and kidney)					
	Whole blood	Liver	Spleen	Lung	Kidney	Heart
0	471.93 ± 55.06	58.42 ± 7.56	112.22 ± 24.69	56.67 ± 9.54	52.01 ± 8.61	59.61 ± 13.38
0.5	439.31 ± 54.98	235.05 ± 19.62	350.46 ± 51.17	60.20 ± 14.84	47.23 ± 9.95	59.56 ± 7.07
3	342.28 ± 68.38	199.22 ± 19.69	353.72 ± 144.36	55.40 ± 11.95	41.93 ± 3.73	66.03 ± 19.40
24	313.44 ± 113.85	226.57 ± 38.78	402.28 ± 187.31	79.25 ± 10.67	48.64 ± 9.36	51.28 ± 4.48
48	266.34 ± 27.49	191.45 ± 33.44	247.70 ± 18.61	71.47 ± 13.58	45.96 ± 4.06	58.56 ± 5.04
96	402.88 ± 96.96	159.99 ± 9.16	176.21 ± 27.11	63.05 ± 1.98	44.29 ± 4.87	51.87 ± 5.37
336	552.05 ± 36.63	89.76	122.68	45.45	55.24	40.08

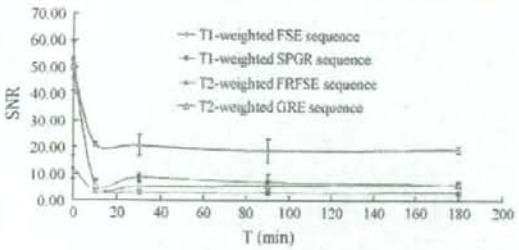

Fig. 2. *In vivo* SNR of liver in normal rats after injection of SPIO-alginate at a dose of 20 μmol Fe/kg. A negative enhancement was observed with T1-weighted, T2-weighted, and T2*-weighted sequences.

3.4. Liver enhancement of SPIO-alginate in normal rat

Fig. 2 showed the liver SNR before and after SPIO-alginate injection on both T1-weighted and T2-weighted images. Compared with unenhanced images ($t = 0$), the SNR decreased at 10 min on T1-weighted FSE images, T1-weighted SPGR images, T2-weighted FRFSE images, and T2*-weighted GRE images, after SPIO-alginate injection, and remained almost stable up to 180 min, respectively. Hence, a remarkable negative enhancement was immediately obtained after the injection of SPIO-alginate.

3.5. MR imaging for rabbit tumor model

Fig. 3 showed the MR signal intensity of liver parenchyma (thick arrow) decreased, however, that of the tumor (fine arrow) did not obviously change and the borderline of the tumor was found more clearly in comparison with that of unenhanced image. The photograph and sections of rabbit VX2 tumor with Perls staining after MR imaging enhanced with SPIO-alginate were shown in Fig. 4. It was evident that there was a single tumor in the liver with the size of about 2.5 cm in accordance with that in MR images in Fig. 3. Iron oxide particles were observed in the normal part of liver rather than in the tumor (Fig. 4).

3.6. MR imaging for rats with primary liver cancer

During the process of establishing primary liver cancer model of rats, eight rats were dead because of hemorrhage in the tumor and poor resistance. In addition, two rats were chosen randomly and identified as cirrhosis at 12 weeks, and four rats were identified as HCC with cirrhosis at 15 weeks from MR imaging and pathological evaluation. Fifteen rats survived at 18 weeks in MR imaging experiment. All the fifteen rats were accompanied with severe cirrhosis, and no HCC was found in any rat on MR images before the injection of SPIO-alginate (pre-SPIO, unenhanced imaging). However, 22 HCCs were found in 11 rats after injection of SPIO-alginate (post-SPIO, enhanced imaging) and four rats were diagnosed as simple cirrhosis even after injection of SPIO-alginate. The SNR_{liver} decreased from 48.95 ± 4.87 at pre-SPIO to 6.43 ± 3.37 at post-SPIO and the $SNR_{cirrhosis}$ from 45.51 ± 11.71 to 23.47 ± 7.52. However, the SNR_{HCC} remained almost stable (45.51 ± 11.71 at pre-SPIO and 40.53 ± 12.98 at post-SPIO). Furthermore, the CNR of HCC increased from zero at pre-SPIO to 17.69 ± 3.69 at post-SPIO and the relative contrast increased from 1.0 at pre-SPIO to 1.79 ± 0.31 at post-SPIO. Hence, the contrast between HCC and liver parenchyma was significantly increased and the detection of HCC was improved.

In Fig. 5, compared with the signal intensity on unenhanced T2*-weighted GRE images, the liver signal intensity of nor-

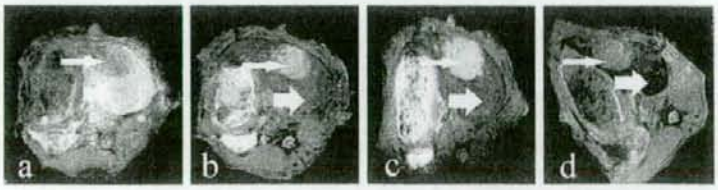

Fig. 3. T2*-weighted FSPGR images (TR/TE, 220 ms/5.2 ms) of xenograft liver cancer in rabbit at (a) 0 min (unenhanced imaging), (b) 10 min, (c) 30 min, and (d) 60 min after intravenous injection of SPIO-alginate at a dose of 20 μmol Fe/kg. After injection of SPIO-alginate, the liver parenchyma (thickness arrow) showed a distinct signal loss, whereas that of the tumor (fine arrow) remained almost unaffected. Hence, the contrast between tumor and liver parenchyma was significantly increased.

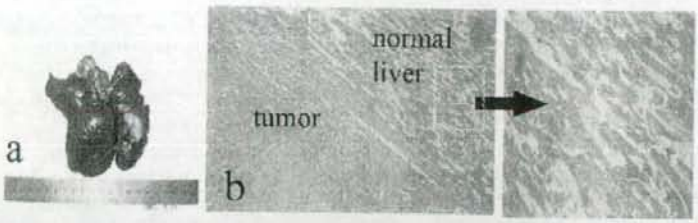

Fig. 4. Photographs (a) and sections of rabbit VX2 tumor with Perls staining (b) after MR imaging enhanced with SPIO-alginate. Iron oxide particles were not found in the tumor part, but in the normal part of the liver (magnification ×10).

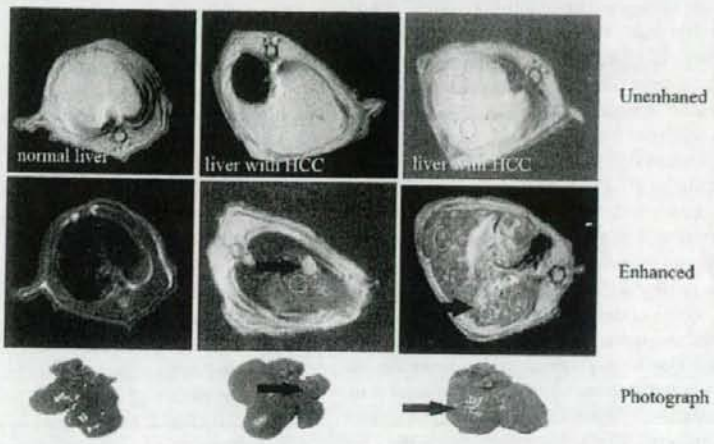

Fig. 5. T2*-weighted GRE images and photographs of liver with primary cancer in rats. No HCC was found on unenhanced images, however, some HCC were found (arrow) on SPIO-alginate enhanced images. The center photograph showed the liver of model rat has one HCC and slight cirrhosis, and the right-hand side photograph showed the liver of model rat has more HCC and severe cirrhosis.

mal rat on enhanced images decreased significantly, slightly decreased for cirrhosis, and almost did not decrease for HCC. Furthermore, there were hyperplastic nodules and some hemorrhage in photographs of model rats' liver. Fig. 6 showed the sections of liver with Perls staining after MR imaging scan, ranging from 2 to 12 h after injection of 20 μmol Fe/kg of SPIO-alginate, which indicated that iron oxide particles were present in normal liver, hyperplastic nodule and hemangioma, rather

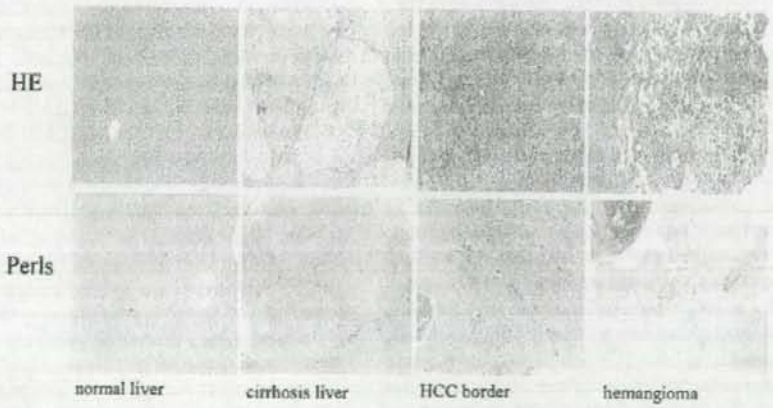

Fig. 6. Light micrograph with HE staining and Perls staining of liver in rats with primary cancer after MR imaging scan within 2–12 h after injection of 20 μmol Fe/kg of SPIO-alginate. According to HE staining, the liver structure of control group was normal, and that of tumor model group accompanied with cirrhosis. Besides HCC, hyperplastic nodule, and hemangioma were identified. As for Perls staining, iron oxide particles were detected in the hemangioma and hyperplastic nodule, rather than in HCC (magnification ×10).

than in HCC. All the livers of model rats were accompanied by cirrohsis according to HE staining. Meanwhile, some HCCs, hyperplastic nodules, and hemangiomas were indentified.

4. Discussion

The alginate used in the study is of pharmaceutical grade which has been approved for oral administration as an inactive ingredient in human. Moreover, sodium alginate was studied for intravenous injection in some animals, and the LD_{50} was described as less than 200 mg/kg for mouse, approximately 100 mg/kg for rabbit (Solandt, 1941), and 1000 mg/kg for rat (Sokov, 1970). In this study, the amounts of sodium alginate used in rats were about 40 mg/kg, which is far less than the LD_{50} (Sokov, 1970). Furthermore, alginate is considered biocompatible and biodegradable in tissues. Alginate has been reported to undergo proton catalyzed hydrolysis which is dependent on time, pH, and temperature (Gombotz and Wee, 1998; Bouhadir et al., 2001; Robitaille et al., 1999). In addition, the chemical composition and the mitogenic contaminants found in alginate are the two main contributors to alginate immunogenicity including cytokine release and inflammatory reactions (Gombotz and Wee, 1998). Hence, the degradatioin of alginate in SPIO-alginate might result in the edema of hepatocytes.

Pharmacokinetics and tissue distribution of SPIO-alginate after intravenous injection were quantitatively studied by determining the iron concentration in blood, serum and tissues. Although it was difficult to differentiate between the endogenous iron and the injected iron, it was reliable to reflect the *in vivo* behavior of SPIO-alginate by subtracting the endogenous iron concentration and this method was used in some studies (Taupitz et al., 2004; Bourrinet et al., 2006). The phenomenon that the blood iron concentration values were under the initial concentration before injection (about 471.9 μg/mL) was observed from about 6 to 48 h after administration of SPIO-alginate, alginate solution and saline, was speculated these might be caused by the several bleedings. After several bleedings, red blood cell count would decrease and therefore there would be a decrease in iron content in blood samples. The blood iron concentration began to increase to initial level at 96 h after injection for both SPIO-alginate, which might be resulted from the fact that SPIO-alginate after uptake by macrophages was degraded by the lysosomes, and then the iron entered the plasma iron pool and was subsequently incorporated into red cell production (Pouliquen et al., 1991; Weissleder et al., 1989).

Since blood loss could significantly decrease red blood count and blood iron concentration, it was better to evaluate the pharmacokinetics of SPIO-alginate in serum, even though the basic serum iron concentration fluctuated according to different rats. In our study, the serum iron concentrations at various time points after injection of alginate solution were in the range of basic serum iron concentration (Table 1). Hence, it indicated that the intravenous injection of alginate solution had no effect on serum iron concentration. We speculated that the COO^- terminals of alginate might not bind the iron in serum. On the other hand, the half-life of SPIO-alginate in serum were 0.27 ± 0.05 h at 109.5 μmol Fe/kg and 0.65 ± 0.22 h at 218.9 μmol Fe/kg in rats in Table 2. C_{max}, $T_{1/2}$, AUC and MRT in serum with the high dose were significantly higher than those of the low dose ($P < 0.05$). After intravenous injection, SPIO-alginate accumulated dominantly in the liver and spleen with a total percentage of more than 90% (Table 3).

As an MR contrast agent, the physicochemical properties including the size of the particle, the charge and the nature of the coating, and the dose will determine the stability, distribution and metabolism of SPIO agents, and then will certainly affect MR imaging (Gupta and Gupta, 2005; Wang et al., 2001; Neuberger et al., 2005). According to the previous studies, the particle size played a very important role. The larger the particles, the shorter the plasma half-life is (Wang et al., 2001). Since SPIO uptake into the RES is related to protein absorption on the particle surface and subsequent opsonization, minimizing the particle size will ultimately reduce particle phagocytosis, finally resulting in a significant increase in plasma half-life and wider biodistribution (Neuberger et al., 2005). Although SPIO-alginate used in this research had a mean core diameter of about 5–10 nm, the big hydrodynamic diameter of 193.8 nm and high negative ξ-potential might explain the fast clearance from blood and the accumulation mostly in the liver and spleen (Table 2). This result was in accordance with the report that the blood half-life of Feumoxides was 6 min and efficiently accumulated in the liver (approximately 80% of the injected dose) and spleen (5–10% of the injected dose) with minutes of administration (Wang et al., 2001). The amount of iron oxide (about 10–20 μmol Fe/kg body weight) for clinical MR imaging is small compared with other MR contrast agents and extensive toxicity studies in animals have indicated no acute or chronic toxicity at doses greater than 100 times the clinical effective dose (Weissleder et al., 1989; Reimer et al., 1995).

For specific characterization of liver lesions, the tissue-specific contrast agent should be located predominantly in one tissue. The distribution of contrast agent in liver is rather complicated, as it can be located in the extracellular space including blood and interstitium, and cellular space including reticuloendothelial cells, hepatocytes and endothelial cells. In our study, Perls staining did not show iron within hepatocytes but mainly within the KCs. Furthermore, the account of SPIO-alginate in the liver peaked at 0.5 h with the dose of 109.5 μmol Fe/kg from quantitative iron concentration (Table 3) and qualitative histology evaluation (Fig. 1). This suggested that SPIO-alginate could not act as an extracelluar agent during the early time points. These results were in accordance with the liver enhancement of SPIO-alginate in normal rat, in which a significant decrease of the liver signal intensity on T1-weighted images at 10 min was observed (Fig. 2). It was reported that positive enhancement on T1-weighted images was observed when the iron particles were extracelluar. When the particles were intracellular, only a negative enhancement was seen (Oswald et al., 1997; Van Beers et al., 2001). It was suggested that the uptake of contrast agents of negative ξ-potential was mediated by scavenger receptors expressed in both Kupffer and liver endothelial cells (Seternes et al., 2001). Compared to KCs, liver endothelial cells were believed to be less effective at metabolizing and degrading particlulate iron (Briley-Sæbø et al., 2004). The half life of SPIO-alginate in

liver at a dose of 109.5 μmol Fe/kg was about 139.1 h (Table 2) and only small iron was observed at 336 h after injection from Perls staining (Fig. 1). Hence, we speculated that there was little or almost no SPIO-alginate in endothelial cell. In sum, the distribution of SPIO-alginate in liver was predominately in KCs, which was just the mechanism of SPIO-alginate to detect liver tumors.

A negative enhancement of the liver was observed on both T1- and T2-weighted images after injection of SPIO-alginate in normal rats (Fig. 2). Compared with the corresponding unenhanced images, SNR on enhanced images decreased by 2.32 times with T1-weighted FSE sequence, 8.02 times with T1-weighted SPGR sequences, 3.88 times with T2-weighted IRFSE sequence, and 8.64 times with T2*-weighted GRE sequence. The negative enhancement on T1-weighted images might be caused by the physical characteristics of the individual nanoparticles. In other words, the high-field magnetization of the iron oxide core could be sufficient to relax water protons effectively, which might attribute to the fact that iron oxide was not simply coated by alginate polymer (Ma et al., 2007). Furthermore, the results also indicated that SPIO-alginate did not agglomerate *in vivo* (Kellar et al., 2002). Meanwhile, the intracellular iron particles mentioned above might be another reason for the negative enhancement on T1-weighted images. On the other hand, the negative enhancement effect of SPIO-alginate on T2- and T2*-weighted images was demonstrated, and GRE images were more sensitive to susceptibility effects than FSE images according to earlier report (Ward et al., 2003).

SPIO-alginate was mainly phagocytosed by liver after intravenous administration as mentioned above. As a result, these particles taken up in liver could accelerate T2 relaxation by creating local inhomogeneities in the magnetic field, causing reduced signal intensity on both T1- and T2-weighted images, but most remarkable decrease on acquisitions with T2*-weighted. In this study, HCC was not found at pre-SPIO on T2*-weighted images, but found at post-SPIO, for the signal intensity of HCC was significantly higher than that of the adjacent liver parenchyma (Fig. 5). Hence, MR imaging with SPIO-alginate enhancement was shown to improve the detection of HCC in the cirrhotic liver compared with unenhanced imaging. Our study confirmed these expectations, as did most published studies of the recent years (Saini et al., 1987; Clement et al., 1991; Nakayama et al., 1998; Imai et al., 2000; Bourrinet et al., 2006).

The efficacy of iron oxide to enhance the transverse relaxation rates ($1/T2^* = R2^*$) in the liver depended upon its initial distribution or uptake into the liver. Factors which may alter the uptake of SPIO particles and the resultant effect on signal intensity include phagocytic activity, clustering of the particles, and local blood flow.

First of all, the change of signal intensity in liver on SPIO enhanced MR imaging is mainly mediated by phagocytic activity. And phagocytic activity is depended on both the number of sinusoidal KCs per unit volume of liver parenchyma (KCs tissue density) and individual KCs function. It is suggested that the number of KCs in dysplastic nodules or in cirrhosis is similar to that in adjacent liver parenchyma, and the number of KCs in HCC decreased as the tumors became less well differentiated (Imai et al., 2000). It has been reported that SPIO-enhanced MR imaging can evaluate the number and function of KCs (Tanimoto et al., 2002). In our studies, iron oxide particles were found in normal liver and hyperplastic nodule, rather than in HCC and VX2 tumor from histological evaluation (Figs. 4 and 6).

It has been reported that the signal intensity changes induced by SPIO may vary according to the spatial distribution of particles and cluster size on relaxation times within KCs in T2*-weighted sequences and T2*-insensitive weighted sequences (Imai et al., 2000). Additionally, large intracellular SPIO clusters produced greater SNR loss on GRE images than small clusters because of the magnetic susceptibility effects relating to fixed-field inhomogeneity. In contrast, small intracellular clusters caused little SNR decrease on T2*-weighted GRE images while the small clusters produced substantial SNR loss on T2-weighted FSE images. This could attribute to T2 shortening mechanisms that were independent of magnetic susceptibility effects but relate to the greater free water interaction made possible by the relatively larger surface area of the small clusters (Tanimoto et al., 1994; Tanimoto et al., 2001). However, the size of the intracellular SPIO clusters depended on individual KC phagocytic function. Hence, impaired phagocytic activity, as in liver cirrhosis, should be associated with a decreased average size of SPIO clusters within KC. In this study, SNR of the normal liver of control rats with T2*-weighted GRE sequence decreased by about eight times on SPIO-enhanced images, while twice as that of the cirrhosis liver of model rats. This result was consistent with those reports that the signal intensity induced by SPIO in patients with liver cirrhosis was less remarkable than that in non-cirrhotic patients (Hundt et al., 2000; Clement et al., 1991; Nakayama et al., 1998). Hemangiomas could show SPIO uptake because of the blood pool effect, although they do not contain KCs (Kim et al., 2002). It was obvious that there were many iron oxide particles stainable in hemangiomas in Fig. 6. Therefore, hemangiomas could not be identified on T2*-weighted MR images.

5. Conclusion

The SPIO-alginate was cleared rapidly from serum with the half-life of 0.27 h at 109.5 μmol Fe/kg and accumulated dominantly in the liver and spleen with a total percentage of more than 90% after intravenous injection. Iron oxide particles in KCs as well as splenic red pulp were observed from histological evaluation in normal rats. The experiments on MR imaging indicated that SPIO-alginate as an MR contrast agent might have the ability to improve detection of liver tumor.

Acknowledgements

This work was supported by funds from National High Technology Research and Development Program of China (2003AA326020), National Basic Research Program of China 2007CB935801, and National Natural Science Foundation of China (30772665).

References

Bouhadir, K.H., Lee, K.Y., Alsberg, E., Damm, K.L., Anderson, K.W., Mooney, D.J., 2001. Degradation of partially oxidized alginate and its potential application for tissue engineering. Biotechnol. Prog. 17, 945–950.

Bourrinet, P., Bengele, H.H., Bonnemain, B., Dencausse, A., Idee, J.M., Jacobs, P.M., Lewis, J.M., 2006. Preclinical safety and pharmacokinetic profile of Ferumoxtran-10, an ultrasmall superparamagnetic iron oxide magnetic resonance contrast agent. Invest. Radiol. 41, 313–324.

Briley-SæbØ, K., Hustvedt, S.O., Haldorsen, A., BjØrnerud, A., 2004. Long-term imaging effects in rat liver after a single injection of an iron oxide nanoparticle based MR contrast agent. J. Magn. Reson. Imaging 20, 622–631.

Clement, O., Frija, G., Chambon, C., Schouman-Claves, E., Mosnier, J.F., Poupon, M.F., Balkau, B., 1991. Liver tumors in cirrhosis: experimental study with SPIO-enhanced MR imaging. Radiology 180, 31–36.

Corot, C., Robert, P., Idee, J.M., Port, M., 2006. Recent advances in iron oxide nanocrystal technology for medical imaging. Adv. Drug Deliv. Rev. 58, 1471–1504.

Gombotz, W.R., Wee, S.F., 1998. Protein release from alginate matrices. Adv. Drug Deliv. Rev. 31, 267–285.

Gupta, A.K., Gupta, M., 2005. Synthesis and surface engineering of iron oxide nanoparticles for biomedical applications. Biomaterials 26, 3995–4021.

Hagar, W., Vichinsky, E.P., Theil, E.C., 2003. Liver ferritin subunit ratios in neonatal hemochromatosis. Pediatr. Hematol. Oncol. 20, 229–235.

Harmut-Hoene, A., Schelenz, R., 1980. Effect of dietary fiber on mineral absorption in growing rats. J. Nutr. 110, 1774–1784.

Hauff, P., Fritzsch, T., Reinhardt, M., Weitschies, W., Lueders, F., Uhlendorf, V., Heldmann, D., 1997. Delineation of experimental liver tumors in rabbits by a new ultrasound contrast agent and stimulated acoustic emission. Invest. Radiol. 32, 94–99.

Hundt, W., Petsch, R., Helmberger, T., Reiser, M., 2000. Signal changes in liver and spleen after Endorem administration in patients with and without liver cirrhosis. Eur. Radiol. 10, 409–416.

Imai, Y., Murakami, T., Yoshida, S., Nishikawa, M., Ohsawa, M., Tokunaga, K., Murata, M., Shibata, K., Zushi, S., Kurokawa, M., Yonezawa, T., Kawata, S., Takamura, M., Nagano, H., Sakon, M., Monden, M., Wakasa, K., Nakamura, H., 2000. Superparamagnetic iron oxide-enhanced magnetic resonance images of hepatocellular carcinoma: correlation with histological grading. Hepatology 32, 205–212.

Kellar, K.E., Fujii, D.K., Gunther, W.H.H., Briley-Saebo, K., Bjornerod, A., Spiller, M., Koenig, S.H., 2002. Important considerations in the design of iron oxide nanoparticles as contrast agents for T1-weighted MRI and MRA. Acad. Radiol. 9, S34–S37.

Kellar, K.E., Fujii, D.K., Gunther, W.H.H., Briley-Saebo, K., Bjornerod, A., Spiller, M., Koenig, S.H., 2000. "NC100150 injection," a preparation of optimized iron oxide nanoparticles for positive contrast MR angiography. J. Magn. Reson. Imaging 11, 488–494.

Kim, J.H., Kim, M.J., Suh, S.H., Chung, J.J., Yoo, H.S., Lee, J.T., 2002. Characterization of focal hepatic lesions with ferumoxides-enhanced MR imaging: utility of T1-weighted spoiled gradient recalled echo images using different echo times. J. Magn. Reson. Imaging 15, 573–583.

Ma, H.L., Qi, X.R., Maitani, Y., Nagai, T., 2007. Preparation and characterization of superparamagnetic iron oxide nanoparticles stabilized by alginate. Int. J. Pharma 333, 177–186.

Ma, H.L., Qi, X.R., Ding, W.X., Maitani, Y., Nagai, T., 2007a. Magnetic targeting after femoral artery administration and biocompatibility assessment of superparamagnetic iron oxide nanoparticles. J. Biomed. Mater. Res. Part A 84A, 598–606.

Nakayama, M., Kamura, T., Kimura, M., Seki, H., Tsukada, K., Sakai, K., 1998. Quantitative MRI of hepatocellular carcinoma in cirrhotic and noncirrhotic livers. Clin. Imaging 22, 280–283.

Neuberger, T., Schöpf, B., Hofmann, H., Hofmann, M., Von Rechenberg, B., 2005. Superparamagnetic nanoparticles for biomedical applications: Possibilities and limitations of a new drug delivery system. J. Magn. Magn. Mater. 293, 483–496.

Oswald, P., Clement, O., Chambon, C., Schouman-Claeys, E., Frija, G., 1997. Liver positive enhancement after injection of superparamagnetic nanoparticles: respective role of circulating and uptaken particles. Magn. Reson. Imaging 15, 1025–1031.

Pouliquen, D., Le Jeune, J.J., Perdrisot, R., Ermias, A., Jallet, P., 1991. Iron oxide nanoparticles for use as an MRI contrast agent: pharmacokinetics and metabolism. Magn. Reson. Imaging 9, 275–283.

Reimer, P., Rummeny, E.J., Daldrup, H.E., Balzer, T., Tombach, B., Berns, T., Peters, P.E., 1995. Clinical results with resovist: a phase 2 clinical trial. Radiology 195, 489–496.

Robitaille, R., Pariseau, J.F., Leblond, F.A., Lamoureux, M., Lepage, Y., Hallé, J.P., 1999. Studies on small (<350 μm) alginate-poly-L-lysine microcapsules. III. Biocompatibility of smaller versus standard microcapsules. J. Biomed. Mater. Res. 44, 116–120.

Saini, S., Stark, D.D., Hahn, P.F., Bousquet, J.C., Introcasso, J., Wittenberg, J., Brady, T.J., Ferrucci J.T.Jr., 1987. Ferrite particles: a superparamagnetic MR contrast agent for enhanced detection of liver carcinoma. Radiology 162, 217–222.

Seternes, T., Oynebraten, I., Sorensen, K., Smedsrod, B., 2001. Specific endocytosis and catabolism in the scavenger endothelial cells of cod (*Gadus morhua* L.) generate high-energy metabolites. J. Exp. Biol. 204, 1537–1546.

Sokov, L.A., 1970. Radioaktivnye Izotopy Vo Vneshnei Sredei Organizine. Atomizdat, Moscow, p. 247.

Solandt, O.M., 1941. Some observations upon sodium alginate. Quart. J. Exp. Physiol. 31, 25–30.

Tanimoto, A., Pouliquen, D., Kreft, B.P., Stark, D.D., 1994. Effects of spatial distribution on proton relaxation enhancement by particulate iron oxide. J. Magn. Reson. Imaging 4, 653–657.

Tanimoto, A., Oshio, K., Suematsu, M., Pouliquen, D., Stark, D.D., 2001. Relaxation effects of clustered particles. J. Magn. Reson. Imaging 14, 72–77.

Tanimoto, A., Yuasa, Y., Shinmoto, H., Jinzaki, M., Imai, Y., Okuda, S., Kuribayashi, S., 2002. Superparamagetic iron oxide-mediated hepatic signal intensity change in patients with and without cirrhosis: pulse sequence effects and Kupffer cell function. Radiology 222, 661–666.

Taupitz, M., Wagner, S., Schnorr, J., Kravec, I., Pilgrimm, H., Bergmann-Fritsch, H., Hamm, B., 2004. Phase I clinical evaluation of citrate-coated monocrystalline very small superparamagnetic iron oxide particles as a new contrast medium for magnetic resonance imaging. Invest. Radiol. 39, 394–405.

Van Beers, B.E., Sempoux, C., Materne, R., Delos, M., Smith, A.M., 2001. Biodistribution of ultrasmall iron oxide particles in the rat liver. J. Magn. Reson. Imaging 13, 594–599.

Wang, Y.X., Hussain, S.M., Krestin, G.P., 2001. Superparamagnetic iron oxide contrast agents: physicochemical characteristics and applications in MR imaging. Eur. Radiol. 11, 2319–2331.

Ward, J., Guthrie, J.A., Wilson, D., Arnold, P., Lodge, P., Toogood, G.J., Wyatt, J.I., Robinson, P.J., 2003. Colorectal hepatic metastases: detection with SPIO-enhanced breath-hold MR imaging-comparison of optimized sequences. Radiology 228, 709–718.

Weinmann, H.J., Ebert, W., Misselwitz, B., Schmitt-Willich, H., 2003. Tissue-specific MR contrast agents. Eur. J. Radiol. 46, 33–44.

Weissleder, R., Stark, D.D., Engelstad, B.L., Bacon, B.R., Compton, C.C., White, D.L., Jacobs, P., Lewis, J., 1989. Superparamagnetic iron oxide: pharmacokinetics and toxicity. Am. J. Roentgenol. 152, 167–173.

Available online at www.sciencedirect.com
ScienceDirect
International Journal of Pharmaceutics xxx (2008) xxx–xxx
INTERNATIONAL JOURNAL OF PHARMACEUTICS
www.elsevier.com/locate/ijpharm

Note

Block copolymer design for stable encapsulation of *N*-(4-hydroxyphenyl)retinamide into polymeric micelles in mice

Tomoyuki Okuda [a], Shigeru Kawakami [a], Masayuki Yokoyama [b], Tatsuhiro Yamamoto [b], Fumiyoshi Yamashita [a], Mitsuru Hashida [a,*]

[a] *Department of Drug Delivery Research, Graduate School of Pharmaceutical Sciences, Kyoto University, Sakyo-ku, Kyoto 606-8501, Japan*
[b] *Kanagawa Academy of Science and Technology, KSP East 404, Sakado 3-2-1, Takatsu-ku, Kawasaki-shi, Kanagawa 213-0012, Japan*

Received 5 October 2007; received in revised form 22 January 2008; accepted 24 January 2008

Abstract

For stable encapsulation of *N*-(4-hydroxyphenyl)retinamide (4-HPR) into polymeric micelles, four types of block copolymers were synthesized with different esterified functional groups: heptyl (C7), nonyl (C9), benzyl (Bz), and phenylpropyl (C3Ph). The stability of 4-HPR encapsulated polymeric micelles was evaluated by measuring the blood concentration of 4-HPR in mice. After intravenous administration of 4-HPR and 4-HPR encapsulated PEG liposomes, the blood concentration of 4-HPR was about 2.8% and 2.2% of the dose/mL, suggesting the rapid release of 4-HPR from PEG liposomes. In contrast, the blood concentration of 4-HPR after intravenous administration of all 4-HPR encapsulated polymeric micelles studied was much higher (about 22–34% of the dose/mL). Among them, the polymeric micelles prepared by block copolymers (Bz) showed the highest blood concentration of 4-HPR. As far as the effects of the level of Bz groups in the block copolymers are concerned, the blood concentration of 4-HPR was enhanced by Bz groups at a level of 72% and 77%, but not by Bz groups at a level of 43% and 51%. These results suggest that 4-HPR is stably encapsulated in polymeric micelles prepared by block copolymers (Bz) but a level of over 72% of Bz groups is needed. These findings will be of value in the future use, design, and development of polymeric micelles for *in vivo* application of 4-HPR.

Keywords: 4-HPR; Fenretinide; Polymeric micelle; Controlled release; Drug delivery systems

N-(4-Hydroxyphenyl)retinamide (4-HPR, fenretinide) is a synthetic retinoid which shows high anti-tumor activity against a variety of malignant cells (Formelli et al., 1996). Although oral administration of 4-HPR has been used in clinical trials so far, its bioavailability is very limited because of its low membrane permeability (Kokate et al., 2006). In addition, intravenous 4-HPR is rapidly eliminated from body (Swanson et al., 1980; Hultin et al., 1986). Therefore, 4-HPR cannot exert a high enough anti-tumor activity because its low blood concentration (Formelli et al., 1993). Raffaghello et al. and Takahashi et al. have reported that 4-HPR encapsulated liposomes containing monoclonal antibody or sterylglucoside mixture exert anti-tumor activities when given intravenously. Therefore, the development of a targeting carrier for 4-HPR is needed in order to obtain potent *in vivo* anti-tumor activity (Raffaghello et al., 2003; Takahashi et al., 2003).

Polymeric micelles prepared by block copolymers, which are composed of both hydrophilic and hydrophobic segments, have been reported to be suitable drug carriers for lipophilic drugs (Kataoka et al., 2001; Gaucher et al., 2005). Recently, we have reported the efficient encapsulation of hydrophobic drugs in polymeric micelles by optimizing the hydrophobic segments with esterified functional groups of poly(ethylene glycol)–poly(aspartate ester) block copolymers (Yokoyama et al., 2004; Kawakami et al., 2005; Watanabe et al., 2006; Chansri et al., 2008). These observations prompted us to investigate the potential use of polymeric micelle formulations by optimizing the hydrophobic segments with esterified functional groups to enhance the blood retention of 4-HPR following intravenous administration. Here, four types of poly(ethylene glycol)–poly(aspartate ester) block copolymers with different esterified functional groups were synthesized to optimize the

* Corresponding author. Tel.: +81 75 753 4545; fax: +81 75 753 4575.
E-mail address: hashidam@pharm.kyoto-u.ac.jp (M. Hashida).

0378-5173/$ – see front matter © 2008 Elsevier B.V. All rights reserved.
doi:10.1016/j.ijpharm.2008.01.044

Please cite this article in press as: Okuda, T., et al., Block copolymer design for stable encapsulation of *N*-(4-hydroxyphenyl)retinamide into polymeric micelles in mice, Int J Pharm (2008), doi:10.1016/j.ijpharm.2008.01.044

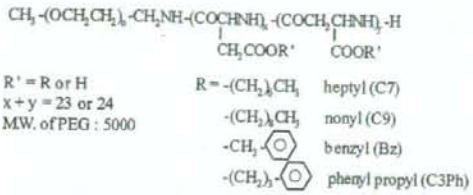

Fig. 1. Schematic illustration of synthesized block copolymers.

stable encapsulation of 4-HPR in the inner core of polymeric micelles (Fig. 1).

Since the *in vivo* drug release from particulate carriers is much higher than that from *in vitro* drug release (Takino et al., 1993; Shabbits et al., 2002), *in vivo* evaluation is important for the development of polymeric micelles for 4-HPR encapsulation. Therefore, the blood concentration of 4-HPR following intravenous administration of 4-HPR encapsulated polymeric micelles into the tail vein of mice was measured using HPLC.

Poly(ethylene glycol)–poly(aspartate ester) block copolymers were obtained by an esterification reaction between a bromide compound and the aspartic acid residue of poly(ethylene glycol)–poly(aspartic acid) block copolymers (Yokoyama et al., 2004). Block copolymers with heptyl, nonyl, benzyl and phenyl propyl groups are abbreviated as C7, C9, Bz and C3Ph, respectively. The esterification level determined by ^{1}H NMR is expressed as a % value following the block copolymer abbreviation. 4-HPR encapsulated polymeric micelles were prepared by a conventional evaporation method modified as described in our previous report (Kawakami et al., 2005). The ratio of block copolymers/4-HPR for their preparation was fixed as 2.5 (weight ratio). As a control, poly(ethylene glycol) modified liposomes (PEG liposomes) were selected to evaluate the potentials of novel polymeric micelle formulations because of their wide use in cancer chemotherapy (Torchilin, 2005).

The physicochemical properties, such as the particle size and zeta potential of the macromolecules, are determining factors for their biodistribution (Takakura and Hashida, 1996). For escape

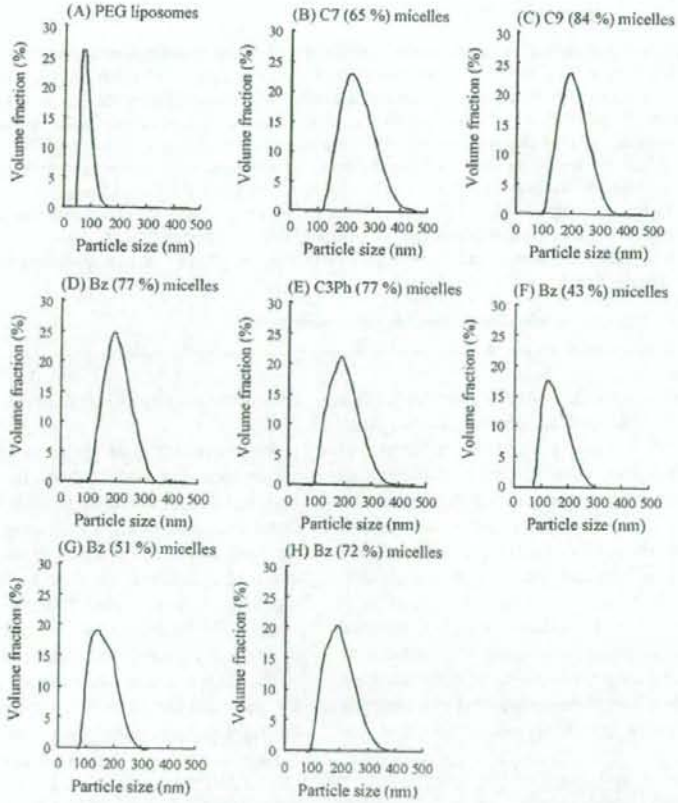

Fig. 2. Size distribution of 4-HPR encapsulated PEG liposomes (A) and polymeric micelles with several types and levels of esterified functional groups (B–H). 4-HPR encapsulated PEG liposomes were composed of hydrogenated soybean phosphatidyl choline (HSPC), cholesterol, distearoylphosphatidylethanolamine-*N*-[methoxy(polyethylene glycol)-2000] (PEG-DSPE), and 4-HPR (33.3:16.7:1.67:1, molar ratio). The ratio of block copolymers/4-HPR for 4-HPR encapsulated polymeric micelles was fixed as 2.5 (weight ratio). They were prepared by a conventional evaporation method modified as described in our previous report (Kawakami et al., 2005).

Please cite this article in press as: Okuda, T., et al., Block copolymer design for stable encapsulation of *N*-(4-hydroxyphenyl)retinamide into polymeric micelles in mice, Int J Pharm (2008), doi:10.1016/j.ijpharm.2008.01.044

Table 1
Zeta potential of 4-HPR encapsulated PEG liposomes (A) and polymeric micelles with several types and levels of esterified functional groups (B–H)

Carrier	Zeta potential (mV)
(A) PEG liposomes	−2.7 ± 1.4
(B) C7 (65%) micelles	−1.7 ± 0.7
(C) C9 (84%) micelles	−2.6 ± 1.0
(D) Bz (77%) micelles	−1.4 ± 1.2
(E) C3Ph (77%) micelles	−0.8 ± 0.8
(F) Bz (43%) micelles	−10.7 ± 1.8
(G)Bz (51%) micelles	−3.1 ± 0.9
(H) Bz (72%) micelles	−2.3 ± 3.2

Each value represents the means ± S.D. (n = 3–4).

of uptake by the reticuloendothelial system and long-term blood retention in the systemic circulation, it is needed that the particle size and zeta potential of PEG modified particulates (liposomes and polymeric micelles) are about <200 nm and weak anion (Oku and Namba, 1994; Nishiyama et al., 2003). Therefore, the mean particle size and zeta potential of 4-HPR encapsulated polymeric micelles were measured using Zetasizer Nano Series (Malven Instruments Ltd., Worcestershire, UK). As shown in Fig. 2 and Table 1, the mean particle size and zeta potential of all 4-HPR encapsulated polymeric micelles ranged from 142 to 225 nm and from −10.7 to −0.8 mV respectively, not dramatically changed irrespective of types and levels of esterified functional groups. The mean particle size and zeta potential of 4-HPR encapsulated PEG liposomes were about 76 nm and −2.7 mV. Thus, 4-HPR encapsulated polymeric micelles and PEG liposomes can avoid uptake by the reticuloendothelial system and enhance the blood retention of 4-HPR after intravenous administration.

After intravenous administration of 4-HPR itself (dissolved in polyoxyethylene hydrogenated castor oil (HCO-60), which was a solubilizing agent) and 4-HPR encapsulated PEG liposomes at 1 h, the blood concentration of 4-HPR was about 2.8% and 2.2% of the dose/mL (Fig. 3), suggesting the rapid release of 4-HPR from PEG liposomes. From the reports of Swanson et al. (1980) and Hultin et al. (1986), the blood concentration of 4-HPR at 1 h after intravenous injection was calculated to be about 3% of the dose/mL, supporting our result. In contrast, the blood concentration of 4-HPR was about 22–34% of the dose/mL after intravenous administration of 4-HPR encapsulated polymeric micelles, suggesting the stable encapsulation of 4-HPR by these types of polymeric micelles. Among them, the polymeric micelles prepared by block copolymers (Bz (77%)) exhibited the highest blood concentration of 4-HPR. Recently, Kataoka et al. reported that doxorubicin can be stably encapsulated in polymeric micelles prepared by poly(ethylene glycol)–poly(β-benzyl-L-aspartate) block copolymers through π–π stacking (Kataoka et al., 2000). Therefore, 4-HPR, which possesses a benzene ring, might be also stably encapsulated in polymeric micelles prepared by block copolymers (Bz (77%)) through this π–π stacking. As far as the effects of the level of Bz groups in the block copolymers are concerned, the blood concentration of 4-HPR was enhanced by Bz groups at a level of 72% and 77%, but not by Bz groups at a level of 43% and 51% (Fig. 4). These results suggest that 4-HPR is stably encapsulated in polymeric micelles prepared by block copolymers (Bz) although a level of over 72% of Bz groups in block copolymers is needed.

Furthermore, long-term biodistribution of 4-HPR after intravenous injection of 4-HPR encapsulated polymeric micelles prepared by block copolymers (Bz (77%)) was evaluated. After intravenous injection of 4-HPR itself (dissolved in HCO-60), 4-HPR was rapidly eliminated from blood circulation and highly distributed in liver (Fig. 5). In addition, all of tissue to blood concentration ratio (K_p) of 4-HPR were increased as time passed, especially K_p value on kidney at 8 h was most high compared with other tissues (Fig. 6). These trends were supported by other report with different intravenous formulation of 4-HPR (Swanson et al., 1980). On the other hand, 4-HPR encapsulated polymeric micelles prepared by block copolymers (Bz (77%)) showed much higher blood concentration of 4-HPR for more than 8 h and lower liver distribution of 4-HPR until 1 h compared with 4-HPR itself (Fig. 5). These results indicated that, 4-HPR encapsulated polymeric micelles prepared by block copolymers (Bz (77%)) showed prolonged circulation of 4-HPR for stable encapsulation of 4-HPR and escape of initial uptake by liver. The mean area under the curve ($AUC_{0\text{-}8\,h}$) in blood of 4-HPR itself

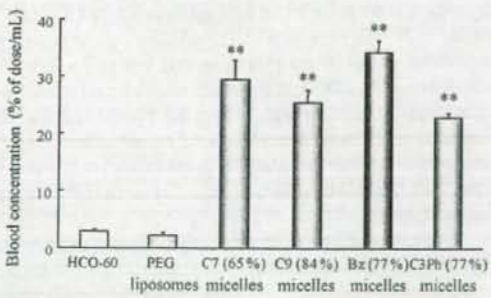

Fig. 3. Blood concentration of 4-HPR itself (dissolved in HCO-60), 4-HPR encapsulated in PEG liposomes, and in polymeric micelles with several types of esterified functional groups at 1 h after intravenous injection into mice at a dose of 5 mg/kg as 4-HPR. Each value represents the means ± S.D. (n = 3–4). **P < 0.01, compared with HCO-60 groups.

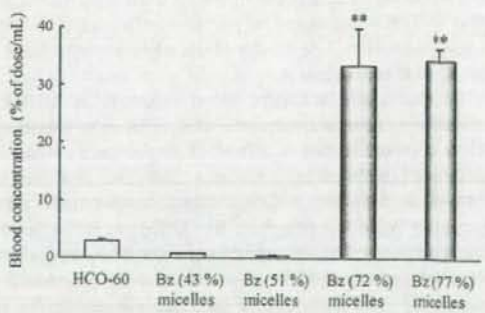

Fig. 4. Effect of level of Bz groups in block copolymers on blood concentration of 4-HPR encapsulated in Bz micelles at 1 h after intravenous injection into mice at a dose of 5 mg/kg as 4-HPR. Each value represents the means ± S.D. (n = 3–4). **P < 0.01, compared with HCO-60 groups.

Please cite this article in press as: Okuda, T., et al., Block copolymer design for stable encapsulation of *N*-(4-hydroxyphenyl)retinamide into polymeric micelles in mice, Int J Pharm (2008), doi:10.1016/j.ijpharm.2008.01.044

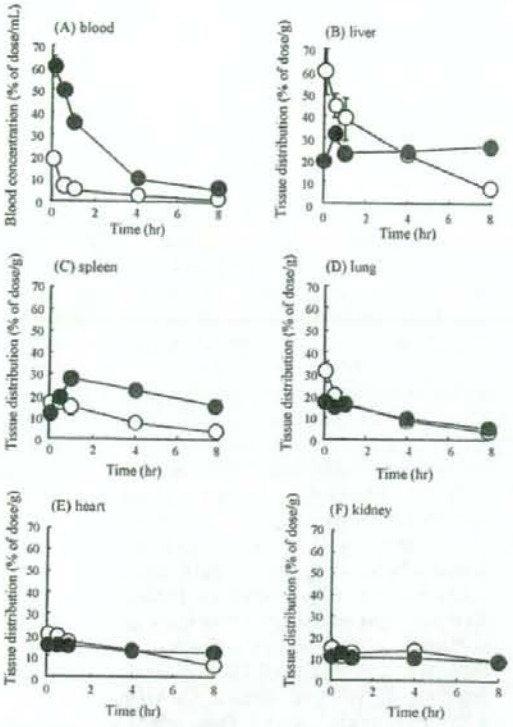

Fig. 5. Blood concentration (A) or tissue accumulation (liver (B), spleen (C), lung (D), heart (E), kidney (F)) of 4-HPR itself (dissolved in HCO-60) (○) and 4-HPR encapsulated in Bz (77%) micelles (●) after intravenous injection into mice at a dose of 5 mg/kg as 4-HPR. Each value represents the mean ± S.D. ($n = 3$–4).

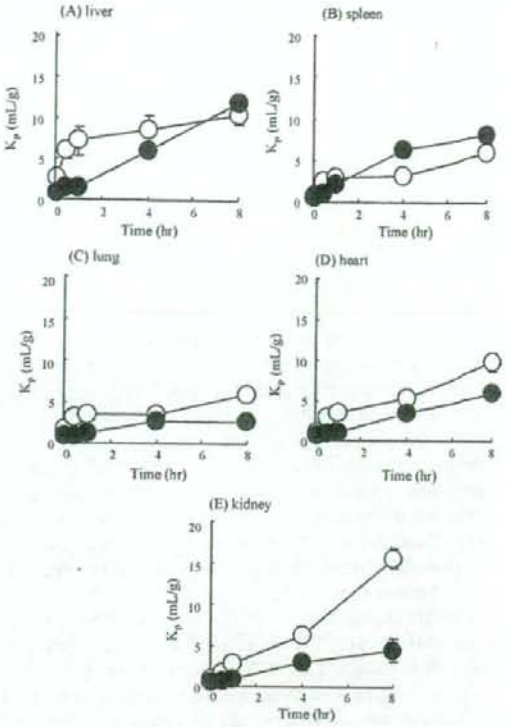

Fig. 6. Tissue to blood concentration ratio (K_p) of 4-HPR in liver (A), spleen (B), lung (C), heart (D), and kidney (E) of 4-HPR itself (dissolved in HCO-60) (○) and 4-HPR encapsulated in Bz (77%) micelles (●) after intravenous injection into mice at a dose of 5 mg/kg as 4-HPR. Each value represents the mean ± S.D. ($n = 3$–4).

and 4-HPR encapsulated in Bz (77%) micelles calculated by the linear trapezoidal rule was 26.4 and 148 (% of dose × h/mL) and its relative AUC ratio was 5.6. Furthermore, K_p in lung, heart, and kidney after intravenous injection of 4-HPR encapsulated polymeric micelles prepared by block copolymers (Bz (77%)) were lower than that of 4-HPR itself (Fig. 6), suggesting that, 4-HPR encapsulated polymeric micelles prepared by block copolymers (Bz (77%)) escaped the transition of 4-HPR from blood to these tissues.

In this study, enhanced blood retention of 4-HPR was achieved by using polymeric micelles prepared by poly(ethylene glycol)–poly(aspartate ester) block copolymers, which were optimized hydrophobic segments with esterified functional groups. In particular, 4-HPR encapsulated polymeric micelles prepared by block copolymers (Bz (77%)) had the highest blood concentration of 4-HPR, which was about 106 μM (34% of the dose/mL) at a dose of 5 mg/kg. As far as the pharmacological effects of 4-HPR on cancer cells are concerned, Kalemkerian et al. have reported that 4-HPR efficiently inhibited the growth of small-cell lung cancer cell line and its IC_{50} values ranged from 0.1 to 3.0 μM (Kalemkerian et al., 1995). The neovascularization formed by solid tumors exhibits some unique features, such as hypervasculature, leaky capillaries and poor lymphatic clearance. These characteristics cause the accumulation of macromolecules in tumors for a long period, known as enhanced permeability and retention (EPR) effects (Matsumura and Maeda, 1986). The spaces in the blood endothelium formed by solid tumors are reported to range from 300 to 4700 nm (Yuan et al., 1995; Hashizume et al., 2000). Since the mean diameter of 4-HPR encapsulated polymeric micelles prepared by block copolymers (Bz (77%)) is about 175 nm, and maximally 342 nm, these may be small enough to pass through the endothelium of solid tumors. These observations led us to believe that 4-HPR encapsulated polymeric micelles prepared by block copolymers (Bz (77%)) could be effective carrier systems for use in future cancer therapy.

In conclusion, poly(ethylene glycol)–poly(aspartate ester) block copolymers with heptyl, nonyl, benzyl and phenyl propyl groups (abbreviated as C7, C9, Bz and C3Ph) were synthesized for stable encapsulation of 4-HPR. It is suggested that 4-HPR is stably encapsulated in polymeric micelles prepared by block copolymers (Bz) although a level of over 72% of Bz groups in the block copolymers is needed for stable encapsulation of 4-HPR. The information we have obtained in this study will be of

Please cite this article in press as: Okuda, T., et al., Block copolymer design for stable encapsulation of *N*-(4-hydroxyphenyl)retinamide into polymeric micelles in mice, Int J Pharm (2008), doi:10.1016/j.ijpharm.2008.01.044

value for the future use, design, and development of polymeric micelles involving the *in vivo* application of 4-HPR.

Acknowledgements

This work was supported in part by Grants-in-Aid for Scientific Research and the Program for Promoting the Establishment of Strategic Research Centers, Special Coordination Funds for Promoting Science and Technology from the Ministry of Education, Culture, Sports, Science, and Technology of Japan, and by the Health and Labour Sciences Research Grants for Research on Advanced Medical Technology from the Ministry of Health, Labour and Welfare of Japan. Yokoyama M. and Yamamoto T. acknowledge support by the Program for Promoting the Establishment of Strategic Research Centers, Special Coordination Funds for Promoting Science and Technology from the Ministry of Education, Culture, Sports, Science, and Technology of Japan.

References

Chansri, N., Kawakami, S., Yokoyama, M., Yamamoto, T., Charoensit, P., Hashida, M., 2008. Anti-tumor effect of all-trans retinoic acid loaded polymeric micelles in solid tumor bearing mice. Pharm. Res. 25, 428–434.

Formelli, F., Clerici, M., Campa, T., Di Mauro, M.G., Magni, A., Mascotti, G., Moglia, D., De Palo, G., Costa, A., Veronesi, U., 1993. Five-year administration of fenretinide: pharmacokinetics and effects on plasma retinol concentrations. J. Clin. Oncol. 11, 2036–2042.

Formelli, F., Barua, A.B., Olson, J.A., 1996. Bioactivities of *N*-(4-hydroxyphenyl) retinamide and retinoyl beta-glucuronide. FASEB J. 10, 1014–1024.

Gaucher, G., Dufresne, M.H., Sant, V.P., Kang, N., Maysinger, D., Leroux, J.C., 2005. Block copolymer micelles: preparation, characterization and application in drug delivery. J. Control Release 109, 169–188.

Hashizume, H., Baluk, P., Morikawa, S., McLean, J.W., Thurston, G., Roberge, S., Jain, R.K., McDonald, D.M., 2000. Openings between defective endothelial cells explain tumor vessel leakiness. Am. J. Pathol. 156, 1363–1380.

Hultin, T.A., May, C.M., Moon, R.C., 1986. *N*-(4-Hydroxyphenyl)-all-trans-retinamide pharmacokinetics in female rats and mice. Drug Metab. Dispos. 14, 714–717.

Kalemkerian, G.P., Slusher, R., Ramalingam, S., Gadgeel, S., Mabry, M., 1995. Growth inhibition and induction of apoptosis by fenretinide in small-cell lung cancer cell lines. J. Natl. Cancer Inst. 87, 1674–1680.

Kataoka, K., Matsumoto, T., Yokoyama, M., Okano, T., Sakurai, Y., Fukushima, S., Okamoto, K., Kwon, G.S., 2000. Doxorubicin-loaded poly(ethylene glycol)–poly(beta-benzyl-L-aspartate) copolymer micelles: their pharmaceutical characteristics and biological significance. J. Control Release 64, 143–153.

Kataoka, K., Harada, A., Nagasaki, Y., 2001. Block copolymer micelles for drug delivery: design, characterization and biological significance. Adv. Drug Deliv. Rev. 47, 113–131.

Kawakami, S., Opanasopit, P., Yokoyama, M., Chansri, N., Yamamoto, T., Okano, T., Yamashita, F., Hashida, M., 2005. Biodistribution characteristics of all-trans retinoic acid incorporated in liposomes and polymeric micelles following intravenous administration. J. Pharm. Sci. 94, 2606–2615.

Kokate, A., Li, X., Jasti, B., 2006. Transport of a novel anti-cancer agent, fenretinide across Caco-2 monolayers. Invest. New Drugs 25, 197–203.

Matsumura, Y., Maeda, H., 1986. A new concept for macromolecular therapeutics in cancer chemotherapy: mechanism of tumoritropic accumulation of proteins and the antitumor agent smancs. Cancer Res. 46, 6387–6392.

Nishiyama, N., Okazaki, S., Cabral, H., Miyamoto, M., Kato, Y., Sugiyama, Y., Nishio, K., Matsumura, Y., Kataoka, K., 2003. Novel cisplatin-incorporated polymeric micelles can eradicate solid tumors in mice. Cancer Res. 63, 8977–8983.

Oku, N., Namba, Y., 1994. Long-circulating liposomes. Crit. Rev. Ther. Drug Carrier Syst. 11, 231–270.

Raffaghello, L., Pagnan, G., Pastorino, F., Cosimo, E., Brignole, C., Marimpietri, D., Montaldo, P.G., Gambini, C., Allen, T.M., Bogenmann, E., Ponzoni, M., 2003. In vitro and in vivo antitumor activity of liposomal Fenretinide targeted to human neuroblastoma. Int. J. Cancer 104, 559–567.

Shabbits, J.A., Chiu, G.N., Mayer, L.D., 2002. Development of an in vitro drug release assay that accurately predicts in vivo drug retention for liposome-based delivery systems. J. Control Release 84, 161–170.

Swanson, B.N., Zaharevitz, D.W., Sporn, M.B., 1980. Pharmacokinetics of *N*-(4-hydroxyphenyl)-all-trans-retinamide in rats. Drug Metab. Dispos. 8, 168–172.

Takahashi, N., Tamagawa, K., Shimizu, K., Fukui, T., Maitani, Y., 2003. Effects on M5076-hepatic metastasis of retinoic acid and *N*-(4-hydroxyphenyl) retinamide, fenretinide entrapped in SG-liposomes. Biol. Pharm. Bull. 26, 1060–1063.

Takakura, Y., Hashida, M., 1996. Macromolecular carrier systems for targeted drug delivery: pharmacokinetic considerations on biodistribution. Pharm. Res. 6, 820–831.

Takino, T., Nakajima, C., Takakura, Y., Sezaki, H., Hashida, M., 1993. Controlled biodistribution of highly lipophilic drugs with various parenteral formulations. J. Drug Target 1, 117–124.

Torchilin, V.P., 2005. Recent advances with liposomes as pharmaceutical carriers. Nat. Rev. Drug Discov. 4, 145–160.

Watanabe, M., Kawano, K., Yokoyama, M., Opanasopit, P., Okano, T., Maitani, Y., 2006. Preparation of camptothecin-loaded polymeric micelles and evaluation of their incorporation and circulation stability. Int. J. Pharm. 308, 183–189.

Yokoyama, M., Opanasopit, P., Okano, T., Kawano, K., Maitani, Y., 2004. Polymer design and incorporation methods for polymeric micelle carrier system containing water-insoluble anti-cancer agent camptothecin. J. Drug Target 12, 373–384.

Yuan, F., Dellian, M., Fukumura, D., Leunig, M., Berk, D.A., Torchilin, V.P., Jain, R.K., 1995. Vascular permeability in a human tumor xenograft: molecular size dependence and cutoff size. Cancer Res. 55, 3752–3756.

Please cite this article in press as: Okuda, T., et al., Block copolymer design for stable encapsulation of *N*-(4-hydroxyphenyl)retinamide into polymeric micelles in mice, Int J Pharm (2008), doi:10.1016/j.ijpharm.2008.01.044

Available online at www.sciencedirect.com
ScienceDirect
Journal of Controlled Release 119 (2007) 262–270
journal of controlled release
www.elsevier.com/locate/jconrel

Optimization of tumor-selective targeting by basic fibroblast growth factor-binding peptide grafted PEGylated liposomes

Takeshi Terada, Miki Mizobata, Shigeru Kawakami, Fumiyoshi Yamashita, Mitsuru Hashida *

Department of Drug Delivery Research, Graduate School of Pharmaceutical Sciences, Kyoto University, Kyoto 606-8501, Japan

Received 5 September 2006; accepted 24 January 2007
Available online 9 February 2007

Abstract

We have previously shown that the peptide, KRTGQYKLC (bFGF), is recognized by fibroblast growth factor (FGF) receptor (FGFR) via binding to basic FGF (bFGF), and is capable of being used for drug delivery to tumors highly expressing FGFR and bFGF. However, although the binding and uptake of the liposomes (bFGFp-liposomes) modified by the peptide increased in the presence of bFGF, the modification induced non-specific uptake. To overcome this problem, here, we prepared bFGFp-liposomes including mPEG-DSPE. The 5 and 10% $mPEG_{5000}$/ and 10% $mPEG_{3000}$/bFGFp-liposomes reduced most of the interaction with erythrocytes and the uptake by macrophages, suggesting the sustained blood circulation of bFGFp grafted PEGylated liposomes. Furthermore, 10% $mPEG_{3000}$/bFGFp-liposomes produced a significant increase in uptake in NIH3T3, A549, and B16BL6 cells with the expression of FGFR following pre-incubation with bFGF, but no increase in CHO-K1 cells lacking FGFR expression. Taken together, these results lead us to believe that bFGFp grafted PEGylated liposomes possess the functions of both PEGylated stealth liposomes and the tumor-targeting liposomes. This strategy could be applied to the development of novel tumor-selective drug delivery systems.

Keywords: Drug delivery system; Liposomes; Targeting; bFGFp-liposomes; Cancer

1. Introduction

Tumor cells, such as melanoma, breast cancer, and prostate cancer, are reported to exhibit overexpression of basic fibroblast growth factor (bFGF) and FGF receptors (FGFR) [1–3]. Furthermore, such tumors have high concentrations of bFGF [4], a multi-functional protein, which has mitogenic, chemotactic, and angiogenic activities and plays an autocrine role in tumor angiogenesis and progression [5–9].

It has been reported that residues 117–126 of bFGF might interact with bFGF itself [10]. Recently, we have shown that the peptide KRTGQYKLC (bFGFp) containing cysteine at the carboxyl terminal of residues 119–126 of bFGF is able to bind to bFGF and is recognized by FGFR via this binding [11]. The binding of bFGFp to bFGF was also higher than that to albumin which is the major serum protein, and the dissociation constant was very low. Based on these findings, we have demonstrated that bFGFp grafted liposomes (bFGFp-liposomes) are specifically taken up by tumor cells highly expressing FGFR via binding to bFGF, suggesting that it could be used as a novel drug delivery carrier to target tumors. However, it was also shown that the non-specific binding of bFGFp-liposomes by bFGFp is high. Therefore, further optimization is needed to reduce the non-specific binding for the in vivo use of bFGFp-liposomes for tumor-specific targeting.

It has been reported that polyethyleneglycol (PEG)-grafted liposomes are not highly recognized by the reticulo-endothelial system (RES) and they remain longer in the blood circulation than conventional liposomes [12–15]. Accordingly, in the design of bFGFp-liposomes, one approach is to conjugate bFGFp to the liposomal PEG terminals. This strategy has been reported to be an effective targeting approach to reduce non-specific binding [16]. However, Savva et al. showed that PEG-grafted liposomes bearing genetically modified recombinant tumor necrosis factor-α on the PEG terminals exhibited rapid

* Corresponding author. Tel.: +81 75 753 4525; fax: +81 75 753 4575.
E-mail address: hashidam@pharm.kyoto-u.ac.jp (M. Hashida).

0168-3659/$ - see front matter © 2007 Elsevier B.V. All rights reserved.
doi:10.1016/j.jconrel.2007.01.018

plasma elimination and high accumulation in liver and spleen [17]. Furthermore, they suggested that not all biological molecules are suitable as targeting ligands when exposed to the grafted PEG extremities of liposomes circulating for long periods. Since bFGFp contains many basic amino residues, the bFGFp-liposomes possess a positive charge on the liposomal surface even if pFGFp is conjugated to the liposomal PEG terminals. The positive charge may induce rapid uptake by RES and non-specific binding with unexpected cells, such as erythrocytes, after intravenous administration.

In the present study, to overcome this problem, we prepared bFGFp-liposomes containing mPEG-DSPE (bFGFp grafted PEGylated liposomes). This mPEG is expected to limit the interactions with RES and other non-target cells. Therefore, we evaluated the inhibitory effects on the uptake by macrophages, used as model cells of the RES, and the interaction with erythrocytes in vitro. Furthermore, the binding of bFGFp grafted PEGylated liposomes to bFGF can induce the specific uptake by the tumor cells expressing FGFRs due to the protrusion of the binding bFGF from the PEG layer.

2. Materials and methods

2.1. Materials

Recombinant human bFGF was obtained from PeproTech EC. (London, UK). Recombinant human FGFR1α (IIIc)/Fc chimera (FGFR1) was purchased from Techne Co. (Minneapolis, MN, USA). Distearoyl phosphatidylcholine (DSPC) was purchased from Sigma-Aldrich Co. (St. Louis, MO, USA). Cholesterol (Chol) and Clear-Sol I were obtained from Nacalai Tesque Inc. (Kyoto, Japan). [^{3}H] CHE was purchased from NEN Life Science Products Inc. (Boston, MA, USA). The peptide KRTGQYKLC (bFGFp) was custom-made by Toray Research Center Inc. (Tokyo, Japan). mPEG$_{3000}$-DSPE was purchased from Avanti Polar Lipids Inc. (Alabama, AL, USA). mPEG$_{3000}$-DSPE and Maleimide-PEG$_{2000}$-DSPE was purchased from NOF Co. Inc. (Tokyo, Japan). All other chemicals were reagent grade products obtained commercially.

2.2. Cell lines

NIH3T3 mouse fibroblasts, A549 human lung cancer cells, and B16BL6 mouse melanoma cells were routinely grown in DMEM medium supplement with 10% FBS, 100 IU/mL penicillin, 100 μg/mL streptomycin, and 2 mM L-glutamine (all from Invitrogen Co., Carlsbad, CA, USA) in 5% CO_2, humidified air at 37 °C. Chinese hamster ovary (CHO)-K1 cells were cultured in Ham's F12 medium supplemented with 10% FBS.

2.3. Synthesis of bFGFp-PEG-DSPE

Synthesis of bFGFp-PEG-DSPE was carried out by the method described previously [11]. Briefly, 28 mg bFGFp (26 μmol) was dissolved in 2 mL 0.1 M HEPES buffer (pH 7.0) then 50 mg maleimide-PEG$_{2000}$-DSPE (17 μmol) and 0.2 mL methanol were added to the bFGFp solution at 4 °C while stirring. The reaction was continued at 4 °C for 2 days. To remove the unreacted bFGFp, the solution was dialyzed against distilled water using a suitable dialysis membrane (3.5 kDa cut-off), and lyophilized. TLC analysis and ninhydrin assay showed the disappearance of free maleimide-PEG$_{2000}$-DSPE and the appearance of bFGFp-PEG$_{2000}$-DSPE, indicating that the reaction had gone to completion. The purity of the synthesized bFGFp-PEG-DSPE was calculated by fluorescamine assay [18] and found to be over 90% on the basis of the bFGFp amino acids. Furthermore, 10 mM L-cysteine solution and the product were mixed at room temperature for 1 h to consume any free maleimide-PEG$_{2000}$-DSPE, followed by dialysis and lyophilization.

Table 1
Lipid composition and mean particle size of liposomes investigated

Lipid composition (molar ratio)	Particle size (nm)*
mPEG-liposomes (DSPC/Chol/mPEG-DSPE= 60:37.5:2.5)	101±1.71
bFGFp-liposomes (DSPC/Chol/bFGFp-PEG-DSPE= 60:37.5:2.5)	100±1.76
1% mPEG$_{3000}$/bFGFp-liposomes (DSPC/Chol/bFGFp-PEG-DSPE/mPEG$_{3000}$-DSPE= 60:36.5:2.5:1)	115±1.99
2.5% mPEG$_{3000}$/bFGFp-liposomes (DSPC/Chol/bFGFp-PEG-DSPE/mPEG$_{3000}$-DSPE= 60:35:2.5:2.5)	113±7.06
5% mPEG$_{3000}$/bFGFp-liposomes (DSPC/Chol/bFGFp-PEG-DSPE/mPEG$_{3000}$-DSPE= 60:32.5:2.5:5)	114±0.651
10 mol% mPEG$_{3000}$/bFGFp-liposomes (DSPC/Chol/bFGFp-PEG-DSPE/mPEG-DSPE$_{3000}$= 60:27.5:2.5:10)	101±1.36
1% mPEG$_{5000}$/bFGFp-liposomes (DSPC/Chol/bFGFp-PEG-DSPE/mPEG$_{5000}$-DSPE= 60:36.5:2.5:1)	116±0.961
2.5% mPEG$_{5000}$/bFGFp-liposomes (DSPC/Chol/bFGFp-PEG-DSPE/mPEG$_{5000}$-DSPE= 60:35:2.5:2.5)	113±1.21
5% mPEG$_{5000}$/bFGFp-liposomes (DSPC/Chol/bFGFp-PEG-DSPE/mPEG$_{5000}$-DSPE= 60:32.5:2.5:5)	106±1.26
10% mPEG$_{5000}$/bFGFp-liposomes (DSPC/Chol/bFGFp-PEG-DSPE/mPEG$_{5000}$-DSPE= 60:27.5:2.5:10)	101±5.02

*The mean particle sizes of the liposomes were measured using a laser light scattering particle size analyzer. Results are expressed as the mean±S.D. of three experiments.

2.4. Preparation of liposomes

Liposomes were prepared by our previously reported method [19–21]. Each lipid mixture (DSPC, Chol, mPEG$_{3000}$-DSPE, and mPEG$_{5000}$-DSPE) was dissolved in chloroform and evaporated to dryness. bFGFp-PEG-DSPE was solved in a mixed organic solvent (chloroform:methanol=1:1) beforehand. [^{3}H] CHE or PE-fluorescein (1 mol %) was added to the liposomes for the uptake study and confocal microscopy, respectively. The dried lipid films were hydrated in PBS, sonicated at 65 °C for 3 min, and

then extruded through 0.2 μm pore size polycarbonate filters. Mean particle diameters were determined by laser light scattering using a Zetasizer Nano ZS instrument (Malvern Instruments, Malvern, UK). All liposomes were similar in size (an average diameter of approximately 100 nm) as shown in Table 1.

2.5. Quartz crystal microbalance (QCM) biosensor system

Binding analysis between bFGF and bFGFp-liposomes was performed with a 27 MHz QCM instrument (AffinixQ, Initium Inc, Tokyo, Japan). bFGF was immobilized on a ceramic sensor chip using an amine coupling reaction. A drop of 5 mM DTDP was applied to a sensor chip to immobilize the DTDP directly on the gold electrode surface of the chip by an Au–thiol interaction. After 24 h, the sensor chip was then activated by adding a coupling solution including 50 mg/mL EDC and 50 mg/mL NHS. Immobilization of bFGF onto the QCM was achieved by coating the surface with 50 μg/mL bFGF solutions for 2 h at room temperature, followed by rinsing with water. To block the activated surface and non-specific binding sites, the surface was exposed to 50 mM Tris buffer (pH 8.0) and the purchased blocking solution (Initium Inc., Tokyo, Japan) for 30 min and then washed with water. After immersing the prepared sensor chip in 8 mL 10 mM HEPES buffer (pH 7.4) containing 150 mM NaCl, with gentle stirring at 37 °C, each sample was added to the buffer and the interaction was investigated by monitoring the alterations in frequency (ΔF) resulting from changes in mass at the electrode surface.

Binding analysis between erythrocytes and each mPEG/bFGFp-liposome preparation was performed with a 27 MHz QCM instrument. Fresh blood from male ICR mice was collected in a heparinized syringe. The mice were obtained from Shizuoka Agricultural Co-operative Association for Laboratory Animals (Shizuoka, Japan). Erythrocytes were washed three times on ice in order to remove serum proteins and resuspended in 10 mM HEPES buffer (pH 7.4) containing 150 mM NaCl. Erythrocytes were immobilized on a ceramic sensor chip by an amine coupling reaction. Briefly, 10% erythrocyte suspension (erythrocyte volume/erythrocyte suspension volume %) was added to the activated surface of the sensor chip by the method described above. After 1 h at 4 °C, the surface was rinsed with PBS. To block the activated surface and non-specific binding sites, the surface was exposed to 50 mM Tris buffer (pH 8.0) containing 150 mM NaCl and the purchased blocking solution (initium Inc., Tokyo, Japan) for 30 min at 4 °C and then washed with PBS. After immersing the prepared sensor chip in 8 mL 10 mM HEPES buffer (pH 7.4) containing 150 mM NaCl, with gentle stirring at 37 °C, each liposome preparation was added to the buffer in the following order: 10 and 5% $mPEG_{5000}$/bFGFp-liposomes, 10% $mPEG_{3000}$-bFGFp-liposomes, and bFGFp-liposomes. The interaction was investigated by monitoring alterations in frequency (ΔF) resulting from changes in mass at the electrode surface.

2.6. Surface plasmon resonance (SPR) spectroscopy assay

SPR measurement was performed using a BIAcore X instrument (BIAcore, Uppsala, Sweden) by our previously reported method [11,22]. FGFR1 was immobilized on the surface of a CM5 sensor chip using the standard amine coupling procedure of the manufacturer. Briefly, the surface of the chip consisting of flow cells 1 and 2 was activated by exposing them to a mixture of 0.05 M *N*-hydroxysuccinimide (NHS) and 0.2 M *N*-ethyl-*N'*-dimethylaminopropyl carbodiimide (EDC) for 7 min. Flow cell 1 was immobilized with FGFR1 in acetate buffer (pH 4.0). The amount of the immobilization was approximately 5000 resonance units (RU). Flow cell 2 was immobilized with the same amount as flow cell 1 by BSA to be used as a blank sensorgram for subtraction of the bulk refractive index background. Finally, the unreacted sites of both immobilized flow cells were blocked with 0.1 M ethanolamine (pH 8.5). All reagents were injected at a flow rate of 5 μL/min.

In the binding measurements, each sample was adjusted to an appropriate concentration by using a buffer (10 mM HEPES, 150 mM NaCl, pH 7.4). Each sample solution was allowed to flow at 20 μL/min for 3 min at 25 °C and dissociated for 3 min. The regeneration of the sensor chip was carried out by injection of 50 mM HCl.

2.7. Cellular uptake study in macrophages

A cellular uptake study in macrophages was performed using our previously reported method [23]. Briefly, five-week-old male ICR mice were obtained from Shizuoka Agricultural Co-operative Association for Laboratory Animals (Shizuoka, Japan). Resident macrophages were collected from the peritoneal cavity of unstimulated mice with serum free RPMI 1640 medium. Washed cells were suspended in RPMI 1640 medium supplemented with serum and plated on 12-well culture plates at a density of 1×10^6 cells/well. After incubation for 2 h at 37 °C in 5% CO_2–95% air, adherent macrophages were washed three times with RPMI 1640 medium to remove non-adherent cells and then cultured under the same conditions. After 48 h incubation, the cells were washed 3-times and incubated with HBSS containing 100 μM (total lipids) of each [^{3}H] liposome form at 37 °C for 2 h. The radioactivity was measured as described above.

2.8. Cellular association experiments

A cellular association study was performed using our previously reported method [11,23]. Briefly, NIH3T3, A549 and CHO-K1 cells were plated on 12-well culture plates at a density of 1×10^5 cells/well. After 24 h incubation, cells were washed three times with Hanks' balanced salt solution (HBSS) and incubated with 100 μM (total lipids) of each [^{3}H] liposome form, with or without pretreatment of 1 μg/mL bFGF, for the indicated time in HBSS at 37 °C. After 5 h, the solution was removed and cells were washed with ice-cold HBSS. Cells were then solubilized with 0.3 N NaOH with 0.1% Triton-X-100 and the radioactivity in the cell lysate was measured using a well-type NaI-scintillation counter (ARC-500, Aloka, Tokyo, Japan). The amount of cellular protein in each cell lysate was estimated using a protein quantification kit (Dojindo Laboratory).

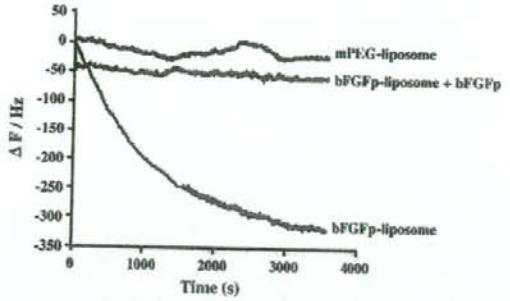

Fig. 1. QCM assay of binding to the immobilized bFGF for mPEG-liposomes and bFGFp (2.5%)-liposomes, with or without 50 μg/mL bFGFp. Two μM (total lipids) liposomes were injected over immobilized bFGF. Each response signal was overlaid and zeroed on the *y*-axis to the average baseline. The start injection time for each form of liposomes was set to zero on the *x*-axis.

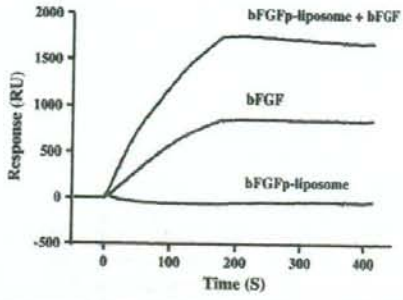

Fig. 2. SPR sensorgrams of binding with the immobilized FGFR1 for 5 μg/mL bFGF, and 100 μM (total lipids) bFGFp (2.5%)-liposomes, with or without 5 μg/mL bFGF. Each sensorgram was overlaid and zeroed on the *y*-axis to the average baseline. The start injection time for each form of liposomes was set to zero on the *x*-axis.

2.9. Confocal microscopic study

The confocal microscopic study was performed using a standard method [24,25]. Briefly, NIH3T3, A549, and B16BL6 cells were seeded on glass coverslips in 12-well plates at a density of 1×10^5 cells/well. After complete adhesion, the cells were washed 3 times with HBSS and incubated at 4 or 37 °C for 5 h with the fluorescent 10% $mPEG_{3000}$/bFGFp-liposomes, with or without the pretreatment of 1 μg/mL bFGF, for 24 h in HBSS. After incubation, the liposome solution was removed, and the cells were washed 3 times with HBSS, followed by fixing with 4% parafolmaldehyde in PBS, and incubating at room temperature for more than 20 min. After washing twice with PBS, the cells were mounted in glycerol:PBS (1:1) containing 2.5% 1,4-diazobicyclo (2,2,2) octane. Images were obtained by confocal laser scanning microscopy (MRC-1024, Bio-Rad, Hercules, CA, USA).

2.10. Statistical analysis

Statistical analysis was performed using Student's paired *t*-test for two groups. Multiple comparisons with the control group were performed by ANOVA with Dunnett's multiple-comparison test. $P<0.05$ was considered to be indicative of statistical significance.

3. Results

3.1. Interaction analysis of bFGFp-liposomes with bFGF

The interaction of bFGFp-liposomes with bFGF was investigated using the QCM biosensor system (Fig. 1). The 27-MHz QCM biosensor system used in this study has a sensitivity of 0.6 ng cm^{-2} of mass change per 1 Hz of frequency decrease [26]. bFGF was immobilized on a sensor chip coated with DTDP by amine coupling. Fig. 1 shows the typical frequency changes for the bFGF-immobilized QCM sensor chip, responding to additions of mPEG-liposomes or bFGFp-liposomes in solution. The addition of mPEG-liposomes produced no change in the frequency (mass). On the other hand, in the case of bFGFp-liposomes, the frequency decreased (mass increased), and the decrease was inhibited by the presence of excess bFGFp. Therefore, the frequency decrease

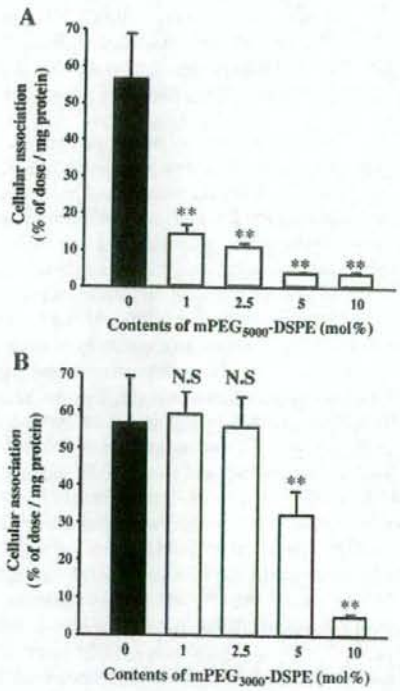

Fig. 3. Effect of the content and length of mPEG-DSPE on the uptake of [^{3}H] mPEG/bFGFp-liposomes (□) by mouse peritoneal macrophages. Peritoneal macrophages were incubated with $mPEG_{5000}$/bFGFp-liposomes (A) and $mPEG_{3000}$/bFGFp-liposomes (B) containing different amounts of mPEG-DSPE at 37 °C for 2 h. The uptake of [^{3}H] bFGFp-liposomes (■) was used as a comparison. Each result represents the mean±S.D. values ($n=3$). Statistical significance was analyzed by Dunnett's test versus bFGFp-liposomes (**$P<0.01$; N.S., not significant).

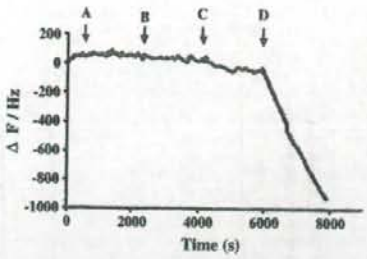

Fig. 4. QCM assay of binding to the immobilized erythrocytes for mPEG/bFGFp-liposomes and bFGFp-liposomes. Two μM liposomes were injected over immobilized erythrocytes in the following order: 10% $mPEG_{5000}$/bFGFp-liposomes (A), 5% $mPEG_{5000}$/bFGFp-liposomes (B), 10% $mPEG_{5000}$/bFGFp-liposomes (C), and bFGFp-liposomes (D).

indicated by the addition of bFGFp-liposomes is consistent with the mass increase due to the binding of bFGFp-liposomes to bFGF via the bFGFp present in the QCM biosensor system.

3.2. The binding of bFGFp-liposomes to FGFR1 via bFGF

Recently, we used SPR spectroscopy to show that BSA modified by bFGFp (bFGFp-BSA) interacts with FGFR1 via binding to bFGF [11]. Here, we confirmed the interaction of bFGFp-liposomes with FGFR1 via binding to bFGF using the same method as in the previous report [11] (Fig. 2). FGFR1 was immobilized on the surface of a CM5 sensor chip by amine coupling. Non-specific binding of an analyte and any change in bulk refractive index were eliminated by immobilizing BSA as a control. Although bFGF showed a significantly high response signal (Fig. 2), no response signal was observed with bFGFp-liposomes. In addition, the response signal of bFGFp-liposomes pre-incubated with bFGF was much higher than that of bFGF itself, suggesting that bFGFp-liposomes pre-incubated with bFGF are capable of binding to FGFR1 via bFGF. These results were in good agreement with our previous report using bFGFp-BSA [11].

3.3. The effect of mPEG-DSPE on the uptake of bFGFp-liposomes by macrophages

Our previous study showed that bFGFp-liposomes exhibit a high degree of unspecific uptake in cells [11]. As shown in Fig. 3, we also found a high uptake by macrophages used as model cells of mononuclear phagocytes in the RES. The high uptake by macrophages would lead to a reduced targeting efficiency to the tumor cells because of the high trapping by RES after intravenous administration. Therefore, we prepared mPEG/bFGFp-liposomes, without or with 1, 2.5, 5, and 10% of $mPEG_{5000}$-DSPE and $mPEG_{3000}$-DSPE, to reduce the non-specific binding and/or uptake. The cellular association in macrophages decreased with an increase in the amount of mPEG-DSPE. In particular, mPEG/bFGFp-liposomes containing 5 or 10% $mPEG_{5000}$-DSPE (Fig. 3 (A)) and 10% $mPEG_{3000}$-DSPE (Fig. 3 (B)) showed a significantly reduced uptake, suggesting prolonged circulation in the body after intravenous administration.

3.4. The effect of mPEG-DSPE on the interaction of mPEG/bFGFp-liposomes with erythrocytes

Furthermore, the effect of mPEG-DSPE on the interaction of mPEG-bFGFp-liposomes with erythrocytes was evaluated using a QCM biosensor system. Fig. 4 shows the typical frequency changes for the isolated erythrocyte-immobilized

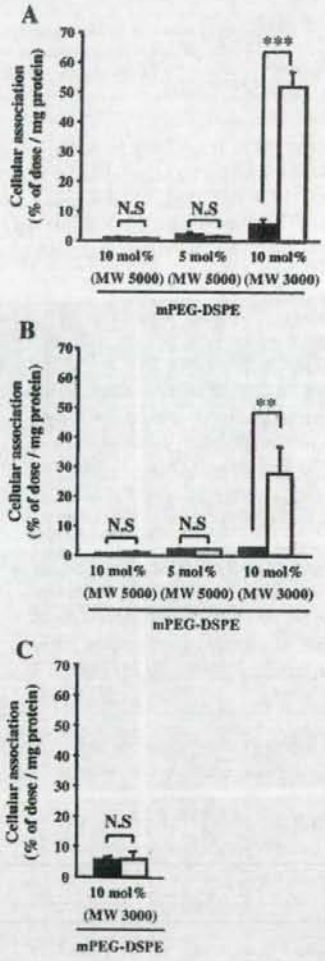

Fig. 5. Effect of bFGF on the cellular association of [^{3}H] mPEG/bFGFp-liposomes by different cells. 10% $mPEG_{5000}$/bFGFp-liposomes, 5% $mPEG_{5000}$/bFGFp-liposome, and 10% $mPEG_{3000}$/bFGFp-liposomes were pre-incubated with bFGF at 37 °C for 24 h. NIH3T3 (A), A549 (B), and CHO-k1 (C) cells were incubated with the mPEG/bFGFp-liposomes without (■) or with (□) the pre-incubation of bFGF at 37 °C for 5 h. Each result represents the mean±S.D. values (n=3). Statistical significance was analyzed by Student's t-test versus each group without the pre-incubation of bFGF (**$P<0.01$; ***$P<0.001$; N.S., not significant).

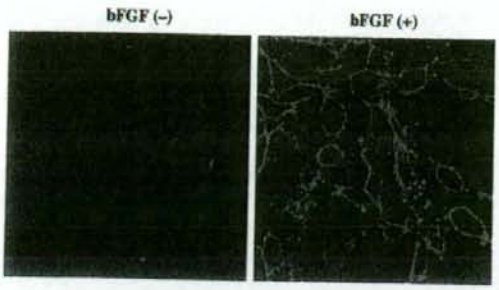

Fig. 6. Confocal microscopy images of the binding of 10% $mPEG_{3000}$/bFGFp-liposomes by NIH3T3 cells. NIH3T3 cells were incubated with 10% $mPEG_{3000}$/bFGFp-liposomes containing 1% PE-fluorescein, without or with the pre-incubation of bFGF at 4 °C for 5 h.

QCM sensor chip, responding to additions of each form of liposomes in the following order: 10 and 5% $mPEG_{5000}$/bFGFp-liposomes, 10% $mPEG_{3000}$/bFGFp-liposomes, and bFGFp-liposomes. The three kinds of mPEG/bFGFp-liposomes indicating the controlled uptake in macrophages exhibited no change in frequency (mass) in the QCM biosensor system, suggesting no interaction with erythrocytes. On the other hand, the frequency decreased (mass increased) following the addition of bFGFp-liposomes. The three mPEG/bFGFp-liposomes are capable of controlling the interaction with erythrocytes via the bFGFp present on the surface of the liposomes.

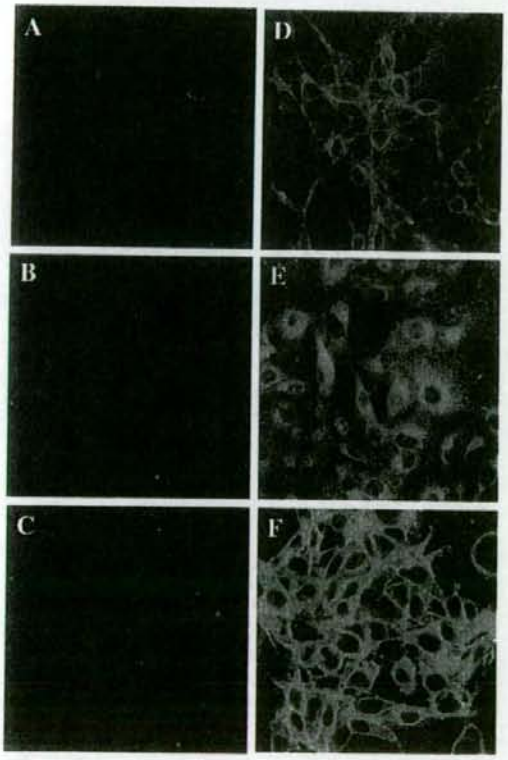

Fig. 7. Confocal microscopy images of the binding and internalization of 10% $mPEG_{3000}$/bFGFp-liposomes by various cells. NIH3T3 (A, D), A549 (B, E), and B16BL6 cells (C, F) were incubated with 10% $mPEG_{3000}$/bFGFp-liposomes containing 1% PE-fluorescein, without (A, B, C) or with (D, E, F) the pre-incubation of bFGF at 37 °C for 5 h.

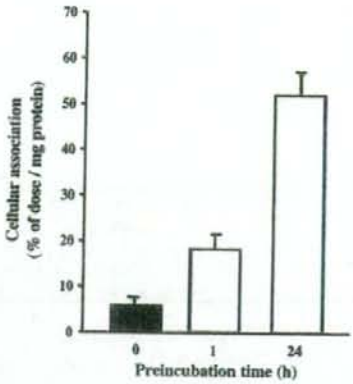

Fig. 8. Effect of the pre-incubation time with bFGF on the cellular association of [^{3}H] $mPEG_{3000}$/bFGFp-liposomes by NIH3T3 cells. 10% $mPEG_{3000}$/bFGFp-liposomes pre-incubated with bFGF for the indicated times were used for the uptake study. Each result represents the mean ± S.D. values (n = 3).

3.5. The effect of bFGF on the uptake of mPEG/bFGFp-liposomes by various cells

The cellular uptake via bFGF of the three mPEG/bFGFp-liposomes was examined (Fig. 5). NIH3T3 and A549 cells express FGFR, and CHO-K1 cells are known to lack these receptors [27]. In these cells with or without FGFRs, the uptake of mPEG/bFGFp-liposomes was almost the same as that in macrophages, suggesting that the each incorporation of 5 or 10%mPEG5000-DSPE and 10% mPEG3000-DSPE is enough to inhibit the non-specific cellular uptake of bFGFp-liposomes. Furthermore, pre-incubation of $mPEG_{3000}$/bFGFp-liposomes with bFGF produced a significant increase in the uptake in NIH3T3 and A549 cells. However, CHO-K1 cells exhibited no such increase while the two PEG_{5000}/bFGFp-liposomes exhibited no uptake in NIH3T3 and A549 cells, even if pre-incubated with bFGF.

3.6. The binding or internalization of $mPEG_{3000}$/bFGFp-liposomes to cells

To further demonstrate the binding of the labeled $mPEG_{3000}$/bFGFp-liposomes with PE-fluorescein via bFGF to cells using confocal microscopy, the liposomes were incubated with NIH3T3 cells at 4 °C. Fluorescent signals of the liposomes pre-incubated with bFGF were observed on the surface of the cells, and these were much stronger than those of liposomes without bFGF (Fig. 6). In addition, the cellular internalization of the liposomes by confocal microscopy was examined in NIH3T3, A549, and B16BL6 cells, all of which are known to

express FGFR (Fig. 7). In all the cells used, the images showed that the liposomes pre-incubated with bFGF were internalized, and the fluorescent signal was stronger than that of the liposomes without bFGF. These results were in good agreement with our previous study of cellular internalization using bFGFp-BSA.

3.7. The effect of the pre-incubation time of $mPEG_{3000}$/bFGFp-liposomes with bFGF on the uptake in NIH3T3 cells

$mPEG_{3000}$/bFGFp-liposomes were incubated with bFGF for 1 and 24 h, and the uptakes in NIH3T3 cells were compared with those of liposomes without bFGF (Fig. 8). Although the incubation for 1 h significantly increased the uptake, incubation of $mPEG_{3000}$/bFGFp-liposomes for 24 h produced a higher increase in uptake. In spite of high association of bFGFp with bFGF, it took a long time to equilibrate the interaction of mPEG3000/bFGFp-liposomes with bFGF. This suggests that the incorporation of mPEG-DSPE in bFGFp-liposomes hinders the interaction of bFGFp with bFGF, and the successful targeting of the tumor takes some time.

4. Discussion

PEGylation provides drug carriers with steric stabilization, subsequently leading to reduce uptake by the RES and prolonged circulation in the body [15,28,29]. Pharmacokinetic analysis and therapeutic studies with tumor-bearing mice have shown that PEG-liposomes have considerable potential as drug carriers for tumor therapy. These liposomes can exploit the "enhanced permeability and retention (EPR)" effect [30–32] for preferential extravasation from tumor vessels, which results in increased liposome accumulation in tumor tissues [33,34]. However, to produce more effective targeting of tumor cells, requires the development of novel liposomes exhibiting both a long circulation by PEGylation and the active targeting by the ligand.

In a previous report, we showed that the peptide KRTG-QYKLC (bFGFp) can interact with FGFR1 via binding to bFGF, and is useful as the targeting ligand for tumor cells [11]. The binding characteristics allow the development of novel PEG-liposomes for tumor therapy. First of all, we confirmed the binding of bFGFp-liposomes to bFGF and FGFR1 by using a QCM biosensor system and SPR spectroscopy, which has been widely used as an instrument to study a variety of biomolecular interactions, including liposome–protein [35,36], DNA–protein [26] and protein–protein [37,38]. All liposomes were prepared with an average diameter of 100–200 nm (Table 1), which has been reported to result in a prolonged circulation time and high tumor accumulation [39,40]. bFGFp-liposomes interacted with bFGF via bFGFp (Fig. 1) and with FGFR1 via binding to bFGF (Fig. 2). These findings agree with our previous report using bFGFp-BSA [11].

To achieve prolonged blood circulation of bFGFp-liposomes in the body, we prepared mPEG/bFGFp-liposomes by adding mPEG-DSPE to bFGFp-liposomes. The steric hindrance of the added mPEG on the surface of bFGFp-liposomes results in a reduction in the non-specific binding caused by the bFGFp present. In this study, we selected two kinds of mPEG-DSPE containing PEG with an MW of 5000 or 3000. Since the MW of the bFGFp-PEG of the synthesized bFGFp-PEG-DSPE is approximately 3000, it appears that the two mPEG-DSPEs have a sufficient PEG to cover the bFGFp present. The high uptake by macrophages and strong interaction with erythrocytes in bFGFp-liposomes, which leads to early elimination from the blood and a low targeting efficiency, were significantly reduced by the addition of 5 and 10% $mPEG_{5000}$/bFGFp- and 10% $mPEG_{3000}$/bFGFp-liposomes (Figs. 3 and 4). These results lead us to believe that these bFGFp grafted PEGylated liposomes would exhibit a prolonged circulation in the body.

In the bFGFp grafted PEGylated liposomes, the targeting to tumor cells via binding to bFGF indicates the success of novel PEG-liposomes exhibiting both prolonged blood circulation and active tumor targeting. In practical terms, we showed that the pre-incubated $mPEG_{3000}$/bFGFp-liposomes with bFGF exhibit specific binding to the cells expressing FGFR (Fig. 5). The addition of 10% $mPEG_{3000}$-DSPE to bFGFp grafted liposomes abolished the binding by the bFGFp present on the liposomal surface, and the binding of bFGF to bFGFp could allow the targeting of tumor cells via FGFR by protrusion of the binding bFGF from the PEG layer. Furthermore, the receptor-mediated internalization demonstrated by confocal microscopy (Fig. 7) would allow the 10% mPEG3000/bFGFp-liposomes to avoid the action of multidrug resistant (MDR) transporters like P-glycoprotein and enhance the pharmacological effects of the antitumor drug as reported recently [41]. We also found that pre-incubation with 10% $mPEG_{3000}$/bFGFp-liposomes enhances the binding on the surface of NIH3T3 cells as shown by an in vitro study at 4 °C (Fig. 6), suggesting that the targeting potential obtained by pre-incubation is not due to the physiological effects of bFGF itself. The difference in uptake between pre-incubation with 10% $mPEG_{3000}$-bFGFp-liposomes for 1 and 24 h also suggests that the targeting is not due to physiological effects (Fig. 8). Furthermore, this result leads us to surmise that targeting via binding to bFGF would take a comparatively long time. Some tumor cells are reported to exhibit overexpression of bFGF and FGFRs [1–3], and such tissues contain high concentrations of bFGF [4]. Taking these findings into consideration, liposomes with a prolonged blood circulation may accumulate in tumor tissues containing high concentrations of bFGF by the EPR effect, and subsequently lead to active targeting via binding to bFGF.

$mPEG_{5000}$/bFGFp-liposomes exhibited no targeting effect on cells even if pre-incubated with bFGF. One possible reason for this is that the long PEG-chains could completely inhibit the interaction with bFGF, or else the bFGFp present could bind to bFGF, and the interaction of the bound bFGF with FGFR was blocked by the long PEG-chains on the liposomal surface. This finding agrees with a previous report showing that the immuno-specific antibody–antigen binding by immunoliposomes conjugated with a monoclonal IgG antibody could be reduced by the addition of PEG with an MW of 2000 [42]. In the case of complicated binding, such as antibody–antigen and bFGF–FGFR, the addition of short PEG-chains could suppress the

targeting effects of ligand-modified liposomes due to steric hindrance.

In the targeting system using ligands such as peptides, species differences area problem as far as successful clinical application is concerned. It has been reported that the homology between murine and human FGF-2 is high (95% homologous) [43]. Moreover, the peptide KRTGQYKL used in the present investigation is completely homologous with both murine and human FGF-2. Therefore, further investigation of this strategy will provide us with information about the potential application to tumor therapy in humans.

In conclusion, we have succeeded in the development of novel PEG-liposomes for tumor targeting. mPEG/bFGFp-liposomes were prepared as novel PEG-liposomes by adding mPEG-DSPE to bFGFp-liposomes capable of targeting tumor cell expressing FGFR via binding to bFGF. The addition of 5 and 10% $mPEG_{5000}$-DSPE and 10% $mPEG_{3000}$-DSPE reduced the uptake by macrophages and interaction with erythrocytes. Furthermore, 10% $mPEG_{3000}$/bFGFp-liposomes exhibited specific targeting of tumor cells via binding to bFGF. Further investigations involving in vivo studies, including the interaction with serum proteins and the targeting efficiency of the local bFGF concentrations in tumor tissue, are needed. However, our results suggest that the bFGFp grafted PEGylated liposomes exhibit both prolonged blood circulation by limiting the transfer to normal tissues and active targeting to cells in the tumor tissues. This strategy could be applied to the development of novel tumor-selective drug delivery systems.

Acknowledgments

This work was supported in part by Grant-in-Aids for Scientific Research from the Ministry of Education, Culture, Sports, Science, and Technology of Japan, by Health and Labour Sciences Research Grants for Research on Advanced Medical Technology from the Ministry of Health, Labour and Welfare of Japan, and by the 21st Century COE Program "Knowledge Information Infrastructure for Genome Science".

References

[1] F. Penault-Llorca, F. Bertucci, J. Adelaide, P. Parc, F. Coulier, J. Jacquemier, D. Bimbaum, O. deLapeyriere, Expression of FGF and FGF receptor genes in human breast cancer, Int. J. Cancer 61 (1995) 170–176.
[2] T. Danielsen, E.K. Rofstad, VEGF, bFGF and EGF in the angiogenesis of human melanoma xenografts, Int. J. Cancer 76 (1998) 836–841.
[3] B. Kwabi-Addo, M. Ozen, M. Ittmann, The role of fibroblast growth factors and their receptors in prostate cancer, Endocr. Relat. Cancer 11 (2004) 709–724.
[4] D. Giri, F. Ropiquet, M. Ittmann, Alterations in expression of basic fibroblast growth factor (FGF) 2 and its receptor FGFR-1 in human prostate cancer, Clin. Cancer Res. 5 (1999) 1063–1071.
[5] R. Halaban, S. Ghosh, A. Baird, bFGF is the putative natural growth factor for human melanocytes, In Vitro Cell. Dev. Biol. 23 (1987) 47–52.
[6] R. Halaban, B.S. Kwon, S. Ghosh, P. Delli Bovi, A. Baird, bFGF as an autocrine growth factor for human melanomas, Oncog. Res. 3 (1988) 177–186.
[7] D.A. Lappi, Tumor targeting through fibroblast growth factor receptors, Semin. Cancer Biol. 6 (1995) 279–288.
[8] A. Compagni, P. Wilgenbus, M.A. Impagnatiello, M. Cotten, G. Christofori, Fibroblast growth factors are required for efficient tumor angiogenesis, Cancer Res. 60 (2000) 7163–7169.
[9] J.K. Dow, R.W. deVere White, Fibroblast growth factor 2: its structure and property, paracrine function, tumor angiogenesis, and prostate-related mitogenic and oncogenic functions, Urology 55 (2000) 800–806.
[10] L. Kinsella, H.L. Chen, J.A. Smith, P.S. Rudland, D.G. Fernig, Interactions of putative heparin-binding domains of basic fibroblast growth factor and its receptor, FGFR-1, with heparin using synthetic peptides, Glycoconj. J. 15 (1988) 419–422.
[11] T. Terada, M. Mizobata, S. Kawakami, Y. Yabe, F. Yamashita, M. Hashida, Basic fibroblast growth factor-binding peptide as a novel targeting ligand of drug carrier to tumor cells, J. Drug Target. 14 (2006) 536–545.
[12] T.M. Allen, G.A. Austin, A. Chonn, L. Lin, K.C. Lee, Uptake of liposomes by cultured mouse bone marrow macrophages: influence of liposome composition and size, Biochim. Biophys. Acta 1061 (1991) 56–64.
[13] D.D. Lasic, F.J. Martin, A. Gabizon, S.K. Huang, D. Papahadjopoulos, Sterically stabilized liposomes: a hypothesis on the molecular origin of the extended circulation times, Biochim. Biophys. Acta 1070 (1991) 187–192.
[14] D. Needham, T.J. McIntosh, D.D. Lasic, Repulsive interactions and mechanical stability of polymer-grafted lipid membranes, Biochim. Biophys. Acta 1108 (1992) 40–48.
[15] K. Maruyama, PEG-immunoliposome, Biosci. Rep. 22 (2002) 251–266.
[16] H. Harashima, T. Ishida, H. Kamiya, H. Kiwada, Pharmacokinetics of targeting with liposomes, Crit. Rev. Ther. Drug Carr. Syst. 19 (2002) 235–275.
[17] M. Savva, E. Duda, L. Huang, A genetically modified recombinant tumor necrosis factor-alpha conjugated to the distal terminals of liposomal surface grafted polyethyleneglycol chains, Int. J. Pharm. 184 (1999) 45–51.
[18] P. Bohlen, S. Stein, W. Dairman, S. Udenfriend, Fluorometric assay of proteins in the nanogram range, Arch. Biochem. Biophys. 155 (1973) 213–220.
[19] S. Kawakami, J. Wong, A. Sato, Y. Hattori, F. Yamashita, M. Hashida, Biodistribution characteristics of mannosylated, fucosylated, and galactosylated liposomes in mice, Biochim. Biophys. Acta 1524 (2000) 258–265.
[20] S. Kawakami, C. Munakata, S. Fumoto, F. Yamashita, M. Hashida, Novel galactosylated liposomes for hepatocyte-selective targeting of lipophilic drugs, J. Pharm. Sci. 90 (2001) 105–113.
[21] C. Managit, S. Kawakami, F. Yamashita, M. Hashida, Effect of galactose density on asialoglycoprotein receptor-mediated uptake of galactosylated liposomes, J. Pharm. Sci. 94 (2005) 2266–2275.
[22] T. Terada, M. Nishikawa, F. Ymashita, M. Hashida, Analysis of the molecular interaction of glycosylated proteins with rabbit liver asialoglycoprotein receptors using surface plasmon resonance spectroscopy, J. Pharm. Biomed. Anal. 41 (2006) 966–972.
[23] T. Terada, M. Iwai, S. Kawakami, F. Yamashita, M. Hashida, Novel PEG-matrix metalloproteinase-2 cleavable peptide-lipid containing galactosylated liposomes for hepatocellular carcinoma-selective targeting, J. Control. Release 111 (2006) 333–342.
[24] N. Skalko, R. Peschka, U. Altenschmidt, A. Lung, R. Schubert, pH-sensitive liposomes for receptor-mediated delivery to chicken hepatoma (LMH) cells. FEBS Lett. 434 (1998) 351–356.
[25] P. Opanasopit, Y. Higuchi, S. Kawakami, F. Yamashita, M. Nishikawa, M. Hashida, Involvement of serum mannan-binding proteins and mannose receptors in uptake of mannosylated liposomes by macrophages, Biochim. Biophys. Acta 1511 (2001) 134–145.
[26] H. Matsuno, K. Niikura, Y. Okahata, Direct monitoring kinetic studies of DNA polymerase reactions on a DNA-immobilized quartz crystal microbalance, Chemistry 7 (2001) 3305–3312.
[27] M. Rusnati, C. Urbinati, E. Tanghetti, P. Dell'Era, H. Lortat-Jacob, M. Presta, Cell membrane GM1 ganglioside is a functional coreceptor for fibroblast growth factor 2, Proc. Natl. Acad. Sci. U. S. A. 99 (2002) 4367–4372.
[28] M. Harada-Shiba, K. Yamauchi, A. Harada, I. Takamisawa, K. Shimokado, K. Kataoka, Polyion complex micelles as vectors in gene therapy—pharmacokinetics and in vivo gene transfer, Gene Ther. 9 (2002) 407–414.
[29] N. Nishiyama, S. Okazaki, H. Cabral, M. Miyamoto, Y. Kato, Y. Sugiyama, K. Nishio, Y. Matsumura, K. Kataoka, Novel cisplatin-incorporated polymeric micelles can eradicate solid tumors in mice, Cancer Res. 63 (2003) 8977–8983.